

**DESIGN AND CONSTRUCTION OF A LOW TEMPERATURE
SCANNING TUNNELING MICROSCOPE**

A Dissertation

by

CHI CHEN

Submitted to the Office of Graduate Studies of
Texas A&M University
in partial fulfillment of the requirements for the degree of

DOCTOR OF PHILOSOPHY

August 2010

Major Subject: Physics

**DESIGN AND CONSTRUCTION OF A LOW TEMPERATURE
SCANNING TUNNELING MICROSCOPE**

A Dissertation

by

CHI CHEN

Submitted to the Office of Graduate Studies of
Texas A&M University
in partial fulfillment of the requirements for the degree of

DOCTOR OF PHILOSOPHY

Approved by:

Chair of Committee,
Committee Members,

Glenn Agnolet
Wenhao Wu
Joseph H. Ross, Jr.
Zhengdong Cheng
Edward S.Fry

Head of Department,

August 2010

Major Subject: Physics

ABSTRACT

Design and Construction of a Low Temperature
Scanning Tunneling Microscope. (August 2010)

Chi Chen, B.S., University of Science and Technology of China, P.R.China

Chair of Advisory Committee: Dr. Glenn Agnolet

A low temperature scanning tunneling microscope (LTSTM) was built that we could use in an ultra high vacuum (UHV) system. The scanning tunneling microscope (STM) was tested on an existing ^3He cryostat and calibrated at room, liquid nitrogen and helium temperatures. We analyzed the operational electronic and vibration noises and made some effective improvements. To demonstrate the capabilities of the STM, we obtained atomically resolved images of the Au (111) and graphite surfaces. In addition, we showed that the stable tunneling junctions can be formed between the Pt/Ir tip and a superconducting thin film PbBi.

We observed the atomic corrugation on Au (111) and measured the height of the atomic steps to be approximately 2.53\AA , which agrees with published values. In our images of the graphite surface, we found both the β atoms triangular structure, as well as the complete α - β hexagonal unit cell, using the same tip and the same bias voltage of 0.2V . The successful observation of the hidden α atoms of graphite is encouraging in regards to the possibility of imaging other materials with atomic resolution using our STM.

We also demonstrated that stable tunneling junctions can be formed at various temperatures. To demonstrate this, the superconducting current-voltage and differential conductance-voltage characteristics of a PbBi film were measured from $1.1K$ to $9K$. From this data, the temperature dependent energy gap of the superconductor was shown to be consistent with the predictions of the Bardeen, Cooper, and Schrieffer (BCS) theory.

Dedicated to my wife

Qin Li

who supported me continuously and made my time in graduate school much easier.

ACKNOWLEDGMENTS

First, I would like to thank my advisor, Dr. Glenn Agnolet, for his continuous support during my doctoral program. I could not have completed the long journey through graduate school without his assistance. He was always there to listen and give advice. He taught me how to do the experiments and express my ideas. He showed me different ways to approach a research problem and the need to be persistent to accomplish any goal. He also helped me to complete this dissertation, as well as the challenging research that lies behind it. It has been an honor to work, live, and learn in his lab. And I would like to thank my committee members: Dr. Wenhao Wu, Dr. Joseph Ross, and Dr. Zhengdong Cheng, for their advice and help.

I would also like to thank the coworkers of Dr. Agnolet's group: Yong Chang, Xin Chen, Lianxi Ma, and Marcus L. Teague, with whom I interacted during several years. In particular, I would like to thank Yong Chang, who gave me much advice and generously shared his experience both in work and life during my first three years of graduate school; Dr. Xin Chen, who broadened my knowledge and gave me valuable assistance on the construction of scanning tunneling microscope; Dr. Lianxi Ma, who helped me greatly when I set up and operated the experimental equipments; undergrad Marcus L. Teague, who helped me to familiarize myself with the lab and western culture.

I need to thank Dr. Huachun Xu for teaching me how to use the SEM. Thanks also goes to Dr. Daya Rathnayaka for helping me prepare the superconducting samples. Thanks also goes to Amanda Schuckman for helping me prepare dodecanethiol samples.

I am grateful to the staff in the machine and electronics shops in the Department of Physics and Astronomy at Texas A&M University. I especially want to thank Thomas Weimar, who instructed me on how to machine many experimental parts, and Steve Payne and James Kirby, who helped me order and fix some electronic equipments.

Last, but not least, I would like to thank my family for their love and support. I am grateful to my parents, Jianjun Chen and Lijun Xiao, for giving me life in the first place, for educating me with aspects from both the arts and the sciences, and for their unconditional support and encouragement to pursue my interests. Thanks to my wife, Qin Li, for her continuous support, for believing in me, and for her enduring patience and understanding.

TABLE OF CONTENTS

	Page
ABSTRACT	iii
DEDICATION	v
ACKNOWLEDGEMENTS	vi
TABLE OF CONTENTS	viii
LIST OF FIGURES.....	x
LIST OF TABLES	xiv
 CHAPTER	
I INTRODUCTION.....	1
A. Scanning Tunneling Microscope (STM).....	1
B. Superconductivity	7
II EXPERIMENTAL APARATUS	14
A. Fiber Optic Interferometer.....	14
B. STM Head.....	18
C. ³ He Cryostat.....	28
D. Electrical Wiring	34
III EXPERIMENTAL PROCEDURES	38
A. Preparation of the STM Head at Room Temperature.....	38
B. Cooling Down the Cryostat	40
C. Data Acquisition	54
IV RESULTS AND DISCUSSION	57
A. Tunneling Noise and Analysis	57
B. Calibration of the STM.....	64
C. Demonstration of Atomic Resolution.....	67
D. Superconductivity Studies.....	75

CHAPTER	Page
V CONCLUSION AND FUTURE WORK.....	80
A. Summary	80
B. Piezoceramic Walker Improvements	81
REFERENCES.....	83
APPENDIX	89
VITA	94

LIST OF FIGURES

FIGURE	Page
1 (a) Schematic illustration of the operational principle of an STM. (b) The tunneling principle. The density of states (DOS) of the sample and the tip are shown in (b), where the filled states are depicted in green. Application of a bias voltage to the sample will either raise or lower the Fermi level of the sample with respect to the Fermi level of the tip. In (b), the sample is negatively biased and allows for the filled states of the sample to tunnel into the empty states of the tip.	3
2 Characteristics of normal-superconductor tunneling junctions. (a) Current – voltage characteristics. (b) Differential conductance – voltage characteristics. Black curves indicate the behavior of a normal-normal junction, the blue curves correspond to $T = 0$, and the red dashed curves are at a finite temperature.	10
3 (a) Measured differential conductance spectra for tunneling (SS) between a superconducting Nb tip and a NbSe ₂ surface; (b) Measured differential conductance spectra for tunneling (NS) between a PtIr tip and a NbSe ₂ surface. Comparison between the SS and NS tunneling spectra, plotted on the same scale, shows the dramatic enhancement in sharpness of the features obtained with a superconducting tip. (Pan et al., 1998).....	12
4 Schematic of the fiber optic interferometer.....	15
5 Working principle of the fiber optic interferometer. (a) The voltage applied on the piezoceramic stack and the reflected PD voltage. (b) The PD voltage versus piezoceramic voltage graph. (c) Illustration of the two reflected beams at the end of the fiber.....	17
6 STM head. (a) Bottom view. (b) Side view (1.4 in in diameter by 2.2 in in height). (1) Sample receptacle. (2) Molybdenum sample plate. (3) Tip. (4) Tip holder. (5) Sapphire prism. (6) Titanium body. (7) Tube holder. (8) Macor insulator. (9) Spring plate. (10) Al ₂ O ₃ plate. (11) Sapphire ball. (12) Shear piezoceramic stack. (13) Piezoceramic tube scanner. (14) Spacer.	20
7 Schematic of working principle of the piezoceramic stacks. (a) The shear orientation of the piezoceramic stack is to the right; as a positive voltage	

FIGURE

Page

	is applied on the top surface of the plate, the plate shifts to the right (dashed line). (b) The shear orientation of the piezoceramic stack is to the left; as a positive voltage is applied on the bottom surface of the plate, the plate still shifts to the right (dashed line). (c) Four piezoceramic plates are epoxied together in the manner shown; as a positive voltage is applied on the top surface of the stack, the stack shifts to the right (dashed line) with four times displacement of a single plate. (d) Al_2O_3 bottom plate deposited with $\sim 100\text{nm}$ gold film. (e) Shape of each piezoceramic plate in piezoceramic stack. Black arrows indicate the shear orientations of the piezoceramic plate; V_+ and V_- indicate the positive and negative voltages applied on the plates; numbers indicate the layers of the stacks.....	23
8	Schematic illustration of the working principle of the coarse approach piezoceramic walker. (a) The sequence of motions of the shear piezoceramic stacks and sapphire prism. (b) The sequence of voltages applied to each piezoceramic stack to produce the motions in (a). (c) Single shear piezoceramic plate. (d) Shear piezoceramic stack with a thin Al_2O_3 plate on the top. Red arrows indicate the shear directions of the plates and “ \pm ” indicate the positive and negative voltage applied on the plate. ((a) and (b), Pan et al., 1999).	25
9	Schematic of homemade ^3He cryostat. (1) Room temperature flange. (2) Room temperature plate. (3) Dewar. (4) 4 K flange. (5) Vacuum can. (6) ^4He pot. (7) ^3He pot. (8) Vacuum can tail. (9) Superconducting magnet. (10) STM head. (11) Spring. (12) Supporting leg. (13) Table top of the vibration isolation table.	29
10	Multi-pin coaxial connectors and banks.....	36
11	Inner and outer view of the 20-pin connector that connects the piezoceramic stacks and the scan tube with the coaxial cables and is mounted on the bottom of STM head.....	37
12	Photographs of the top and bottom details of the STM (scale in centimeters) and photograph of the control panels for all thermometers and heaters.	39
13	Graphs of the liquid helium boil off rate. The liquid helium level drops at a constant rate over time.	53
14	Schematic of the data acquisition circuit.....	55

FIGURE	Page
15 Current noise density measured at different scanning speed or different scanning area. (a) Fixed scanning area with different scanning speeds. (b) Fixed scanning speed with different scanning areas.....	58
16 Current noise density measured at different current setpoints or different bias voltages. (a) Fixed tip-sample separation with different bias voltage-current setpoint pairs. (b) Fixed current setpoint with different bias voltages.....	60
17 (a) The structure of the tip holder. (b) Current noise levels. The black curve is the background noise, the brown curve is the noise with the previous tip holder and tip cable, the red curve is the noise with the new tip holder and tip cable.	63
18 Room temperature calibration of the motion in the x and y directions. (a) Topography of the standard calibration surface. (b) Detailed view of one standard “ball”. (c) Calibration measurements for the STM scanning tube in the x and y directions. Setting the x and y coordinate parameters in the SPM 32 to be $\Delta x/\Delta V = \Delta y/\Delta V = 90 \text{ \AA}/V$, the average size of one ball is $157.5nm$ which is very close to the expected size of $160nm$	66
19 Thin Au (111) film on mica at room temperature. (a) Multi-layers of the Au (111) surface. (b) Detailed view of some of the layers. (c) After setting the z coordinate, parameter in the SPM 32 to be $\Delta z/\Delta V = 24 \text{ \AA}/V$, the height of one atomic step is 2.53\AA which is very close to the published value of 2.5\AA	68
20 (a) Crystal structure of graphite. The unit cell is shaded in green, (Stefen et al., 2003). (b) Measuring the average distance between two β atoms....	70
21 STM images of graphite in constant height mode with the same tip and the same bias voltage of $0.2V$. (a) The hexagonal surface unit cell has two types of carbon atoms, α (white) and β (red), in its basis but here only the β atoms are observed to form a triangular lattice. (b) Both atoms are observed and the hexagonal carbon rings are clearly visible.	74
22 Topography and superconducting energy gap of PbBi film. (a) Constant current mode topography images with different resolutions at $4.17K$. (b) Current-voltage characteristics at $2.09K$, the superconducting energy gap can be directly observed from the graph.....	76

FIGURE	Page
23	Measurements of the current and conductance of a PbBi film at different temperatures. The superconducting phenomena clearly disappear when the temperature is over $7.8K$. (a) Current versus voltage curves. The superconducting energy gap decreases as the temperature is increases. (b) Differential conductance versus voltage curves. The depth of the depressed conductance decreases as the temperature increases.
	78

LIST OF TABLES

TABLE	Page
I Room Temperature Stepsizes of the Piezoceramic Walker	27
II Shielded Wiring to Two Multi-Pin Connectors	36
III Wiring to a 20-Pin Connector on the STM Head	37
IV Nominal Resistance Values at Room Temperature.....	41
V Nominal Resistance Values at Liquid Nitrogen Temperature.....	42
VI Nominal Resistance Values at Liquid Helium Temperature.....	43

CHAPTER I

INTRODUCTION

A. Scanning Tunneling Microscope (STM)

In 1982, Gerd Binnig and Heinrich Rohrer [1, 2] were awarded the Nobel Prize for their invention of the scanning tunneling microscope (STM) with which one can image a metallic surface with atomic resolution. In addition to imaging surface topography, the STM allows one to measure the local electron density of state (LDOS) with exceptional spatial resolution. Over the years, the STM has become a very powerful tool to investigate a wide range of materials and phenomena. There are several well known designs which are used widely, the Besocke or “beetle” design by Besocke [3], the coaxial inertial slider or “slip-stick” design by Lyding [4] and Renner [5], and the “friction motor” design by Pan [6].

Certain types of tunneling measurements, such as studies of superconducting materials, require a very low temperature environment for the STM. Consequently, many scientists have developed STMs that can operate at low temperatures. Early low temperature STMs were mostly housed in conventional ^4He cryostats working at $T \geq 4.2\text{ K}$ [7] (in a few cases down to 1.5 K via a pumped ^4He pot [8, 9]), and were generally cooled by exchange gas. However, some experiments required a very clean

This dissertation follows the style of Surface Science.

environment and so combining low temperatures and ultra high vacuum (UHV) [10, 11] became a new challenge for the STM community, because these system were inherently more complex with the added difficulty of cooling the STM without coupling to mechanical vibrations. In order to study ultralow-temperature phenomena with enhanced energy resolution, a few groups have developed sub-Kelvin systems by inserting the STM into ^3He or dilution refrigerators. Pan et al. [6] reached 240mK with a ^3He cryogenic vacuum, Kugler et al. and Wiebe et al. reached around 300mK with a ^3He UHV [12-14]. Compared to a ^3He cryostat, dilution refrigeration offers the advantage of reaching temperatures on the order of 50mK [15-18]. However, cooling down the sample and the STM below 100mK is very difficult and requires an even more complex design in the dilution refrigerator. Moreover, for maximal flexibility and short turnaround times, an easy *in situ* access to the STM for tip and sample exchange [6, 8, 9, 12], as well as *in situ* tip and sample conditioning [11, 13-15], is necessary. Magnetic fields impose further considerable size and materials constraints. For example, the STM should be nonmagnetic and fit within the magnet coil [6, 8-10, 12-16, 18].

The basic principle of the STM is based on the concept of the quantum tunneling of electrons (Figure 1a). When the atomically sharp conducting tip, typically made of Au, W, Ir, and PtIr, is brought to within a few Angstroms of the metallic or semiconducting sample surface and a bias voltage is applied between the tip and the sample; electrons will

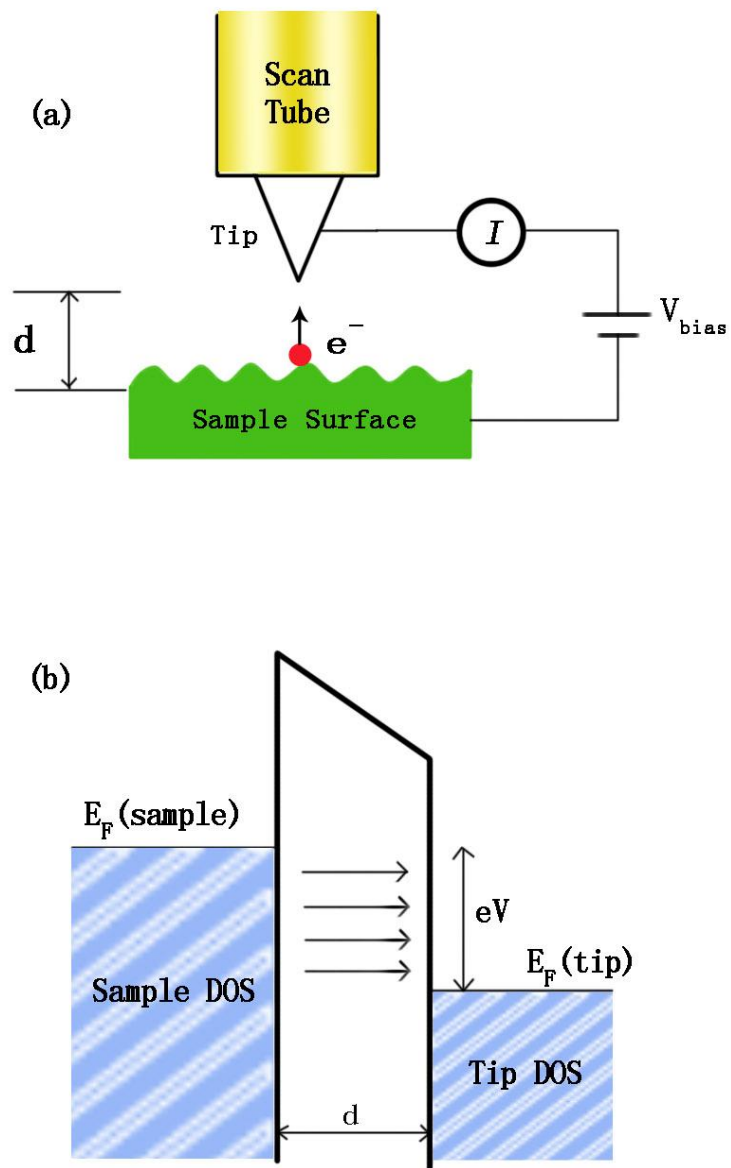


Figure 1. (a) Schematic illustration of the operational principle of an STM. (b) The tunneling principle. The density of states (DOS) of the sample and the tip are shown in (b), where the filled states are depicted in blue. Application of a bias voltage to the sample will either raise or lower the Fermi level of the sample with respect to the Fermi level of the tip. In (b), the sample is negatively biased and allows for the filled states of the sample to tunnel into the empty states of the tip.

tunnel through the vacuum gap resulting in a small tunneling current typically in the nano-Ampere range. The tip is mounted on a piezotube that can move the tip parallel to the surface (x and y directions) as well as perpendicular to the surface (z direction). As the tip is scanned across the sample surface, the tunneling current $I(x, y)$, which depends on the tip-surface separation and tip-surface interaction, is measured as a function of the x and y coordinates.

A scanning tunneling microscope has two working modes to collect topographic and spectroscopic data on the sample surface. In the constant current mode, one adjusts the surface-tip separation (z-direction) via a feedback loop system to maintain a constant tunneling current. If the scan area is essentially flat, the tip-surface separation will also remain constant. By recording the control signal for the z-motion as the tip is scanning across the sample, an image of the topography of the sample surface is produced. Because the tip follows the corrugations of the sample surface at a constant separation, the scan speed is limited by the feedback loop bandwidth. In the constant height mode, the bias voltage and the z-position of the tip remain constant (the feedback loop is turned off). The tunneling current only depends on the tip-surface separation and is recorded as a function of the x and y coordinates to reflect the surface topography. In this mode, the scan speed can be fast, but the scan area is restricted because it is possible for the tip to crash into the sample due to the corrugation (larger than a few angstroms) of the larger scan area. In this

mode, one can also measure the tunneling current or differential conductance at a specific location as a function of the bias voltage. Because the tunneling current flows through a very small region on the order of 5\AA in diameter, the STM is capable of directly measuring changes in the local electronic structure caused by surface irregularities such as impurities, steps and defects.

The origin of the image contrast can be seen by examining the equation for the tunneling current. Based on the WKB approximation [19], the tunneling current can be expressed as,

$$I = \int_0^{eV} \rho_s(r, E) \rho_t(r, \pm eV \mp E) T(E, eV, r) dE \quad (1.1)$$

where $\rho_s(r, E)$ and $\rho_t(r, E)$ are the density of states of the sample and the tip at location r and energy E , the upper signs correspond to a positive sample bias ($eV > 0$) and the lower signs correspond to a negative sample bias ($eV < 0$), and $T(E, eV, r)$ is the tunneling transmission probability. Assuming the bias voltage is smaller than the work function of both the tip and sample, an estimate of the tunneling current is $I = CV \exp(-D\sqrt{\phi}d)$ [20], where C and D are constants, V is the bias voltage, $\phi(eV)$ is the tunnel barrier height (work function of the tip or sample relative to the Fermi level, E_F , depending on the direction of tunneling) and d (\AA) is the distance between the tip and surface. Because the tunneling current decreases exponentially with the tip-surface

separation d , the STM is extremely sensitive to the surface corrugation. For a typical metal ($\phi \sim 5\text{eV}$), the tunneling current will decrease by about one order of magnitude as the tip-surface separation increases by one Angstrom.

As one can see from Eq. 1.1, the tunneling current, I , is proportional to the electronic density of states (DOS) of the tip and sample evaluated at the location of the tip. Moreover, one can show that the first derivative of the tunneling current with respect to bias voltage, dI/dV , only depends on the local density of state (LDOS) within eV above or below the Fermi level. Therefore, in addition to providing the topography of a surface, the STM is capable of measuring the LDOS by recording the tunneling current as the bias voltage is ramped at a fixed tip position. The differential conductance, dI/dV , can be easily obtained using a lock-in amplifier technique. If a small modulation voltage is added to the bias voltage, the current will have a component at frequency ω that is proportional to dI/dV as can be seen in the expansion of the current in a Taylor series,

$$I(V_{DC} + \Delta V \cos(\omega t)) = I(V_{DC}) + \Delta V \cos(\omega t) \left. \frac{dI}{dV} \right|_{V=V_{DC}} + O(\Delta V^2) \quad (1.2)$$

More details are described in Chapter III.

The LDOS near the Fermi level E_F can be modified by adsorbates, such as impurities, thin oxide films, and surface metal oxides, that are on the metal surface. These changes result from the interaction of the adsorbate DOS with the surface DOS. Lang [21,

22] using a simple perturbative approach showed that the STM image of a single, individual adsorbate depends on the LDOS at E_F induced by the adsorbate. If the adsorbate increases the LDOS at E_F , it will appear as a protrusion on the image; and if the adsorbate depletes the LDOS, it will appear as a hole. This effect was demonstrated in STM images of individual Xe atoms absorbed on a Ni (110) surface [23]. These images demonstrate that even though the atomic resonance of a Xe atom is several eV 's above the Fermi level, it may nevertheless make a major influence on the LDOS. Electron transport through double barrier molecular junctions was reported recently using a STM [24]. The tunneling current was established by positioning the STM tip over individual molecules (CuPc and MnP) absorbed on an ultrathin (about 5 \AA) insulating Al_2O_3 film grown on a NiAl (110) surface. This shows that an STM also can provide a topography map of insulating adsorbates and thin films.

B. Superconductivity

Superconductivity was discovered in 1911 by H. Kamerlingh Onnes in Leiden, who observed that the electrical resistance of various metals; such as mercury, lead, and tin; disappeared completely below a critical temperature, T_c , characteristic of that material. This is the first traditional hallmark of superconductivity, which is the prerequisite for most potential applications, such as high-current transmission lines or high-field magnets. The next hallmark to be discovered in 1933 by Meissner and

Ochsenfeld was perfect diamagnetism. They found that not only is an externally applied magnetic field excluded from a superconductor, but that a magnet field is also expelled from an originally normal sample as it is cooled through T_c .

These two basic electro-dynamic properties, which give superconductivity its unique interest, was well described in 1935 by the brothers F. and H. London with two equations [25] governing the microscopic electric and magnetic fields: $E = \frac{\partial}{\partial t}(\Lambda J_s)$, $h = -c\nabla \times (\Lambda J_s)$, where $\Lambda = \frac{4\pi\lambda_L^2}{c^2} = \frac{m}{n_s e^2}$, n_s is the number density of superconducting electrons, and λ_L is the penetration depth. The first equation describes the perfect conductivity, because any electric field accelerates the superconducting electrons rather than simply sustaining their velocity against the resistance as in a normal conductor. Combining the second London equation with the Maxwell equation, $\nabla h = 4\pi J / c$, leads to the equation, $\nabla^2 h = h / \lambda_L^2$. This implies that a magnetic field is exponentially screened from the interior of a superconductor sample with a penetration depth λ_L .

Daunt and Mendelssohn [26] suggested a concept that dramatically helped to understand superconductors, an energy gap between the ground state and the first quasi-particle excitations of the. In 1957, Bardeen, Cooper, and Schrieffer published their famous theory (BCS theory) [27] that became a universal basis for describing superconductors. In the BCS theory, even a weak attraction can bind pairs of electrons,

called Cooper's pair, into a bound state and that the energy gap $E_g(T) = 2\Delta(T)$ is the minimum energy that is required to break a pair, creating two quasi-particle excitations. This $\Delta(T)$ was predicted to increase from zero at T_c to a limiting value $E_g(0) = 2\Delta(0) = 3.528kT_c$ at zero Kelvin. As a function of temperature, $\Delta(T)$ is nearly constant until a significant number of quasi-particles are thermally excited as T approaches T_c . Near T_c $\Delta(T)$ drops to zero with a vertical tangent, approximately as

$$\frac{\Delta(T)}{\Delta(0)} \approx 1.74 \left(1 - \frac{T}{T_c}\right)^{1/2} \quad (1.3)$$

where $T \approx T_c$ [28].

Giaever [29] first introduced the technique of electron tunneling as a means to examine the superconducting density of states in the BCS theory. He formed a planar junction with a superconductor film and a normal metal separated by an insulating barrier and showed that the tunnel current and differential conductance has a functional dependence on voltage which reflects the BCS quasi-particles density of states, as shown in Figure 2. The quantitative formulas of the tunneling current and differential conductance for a normal-superconductor junction were established by McMillan and Rowell [30],

$$I_{ns} = \frac{G_{nn}}{e} \int_{-\infty}^{\infty} \frac{N_s(E)}{N(0)} [f(E) - f(E + eV)] dE \quad (1.4)$$

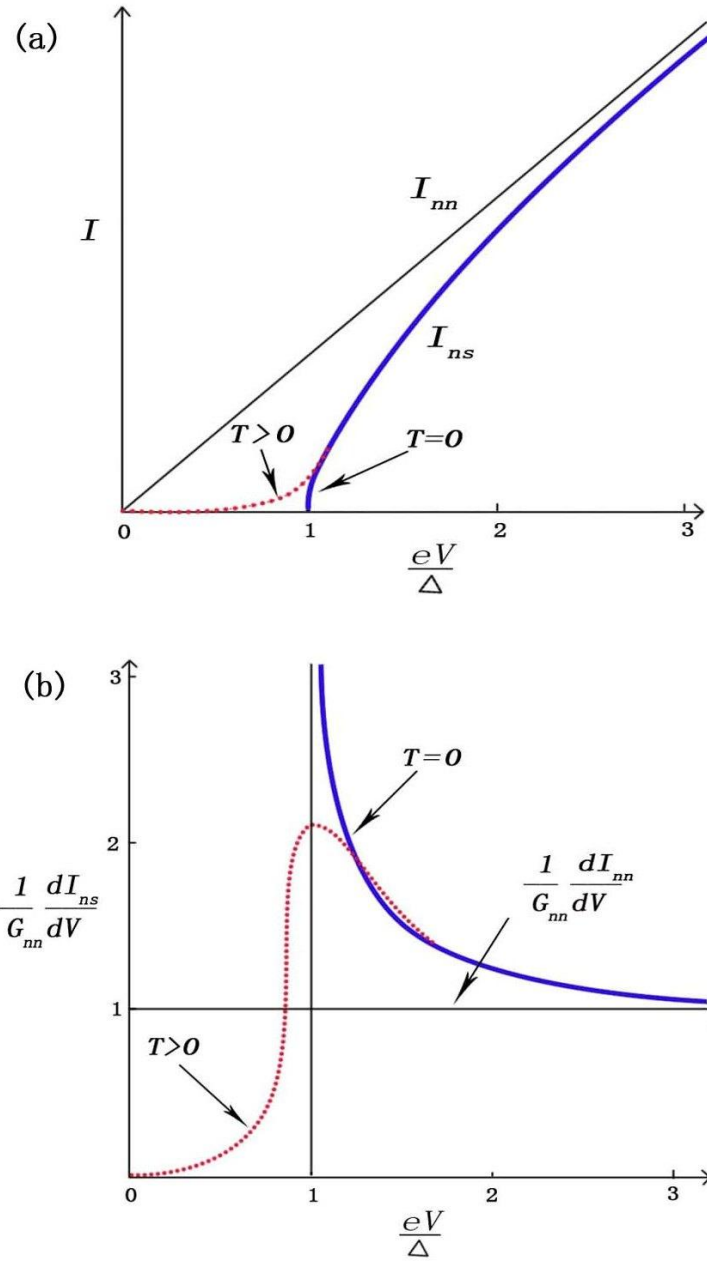


Figure 2. Characteristics of normal-superconductor tunneling junctions. (a) Current – voltage characteristics. (b) Differential conductance – voltage characteristics. Black curves indicate the behavior of a normal-normal junction, the blue curves correspond to $T = 0$, and the red dashed curves are at a finite temperature.

$$G_{ns} = \frac{dI_{ns}}{dV} = G_{nn} \int_{-\infty}^{\infty} \frac{N_s(E)}{N(0)} \left[-\frac{\partial f(E + eV)}{\partial(eV)} \right] dE \quad (1.5)$$

where $G_{nn} = dI_{nn} / dV$ is the normal conductance, $N_s(E)$ is the superconducting density of states at energy E , $N(0)$ is the electric density of states at the Fermi surface, and f is the Fermi function. Figure 2 shows these curves at $T = 0$ and $0 < T \ll T_c$.

Since the inception of the scanning tunneling microscope, STM has been proved to be a useful tool to study the superconductivity. In 1985 A. L. de Lozanne, et al. reported the first images of spatial variations of superconductivity on length scales as small as 13 nm [31]. Subsequently, many scientists have used STMs with non- superconducting tips to successfully study the local electronic properties of super- conducting samples [32, 33]. In 1998, S. H. Pan; el at used STMS with superconducting tips to achieve atomically resolved microscopy and spectroscopy [34]. By comparing the tunneling spectra from superconductor-superconductor (SS) and normal-superconductor (NS), they demonstrated that the sharpness of the features was dramatically enhanced in the SS mode (Shown in Figure 3).

For many years, 30 K was thought to be the highest possible theoretical transition temperature T_c in many years. The first high T_c superconductor, La-Ba-Cu-O with $T_c = 30K$, was discovered by Bednorz and Müller [35], for which they won the Nobel Prize in Physics in the following year. After that, many scientists have studied a variety of

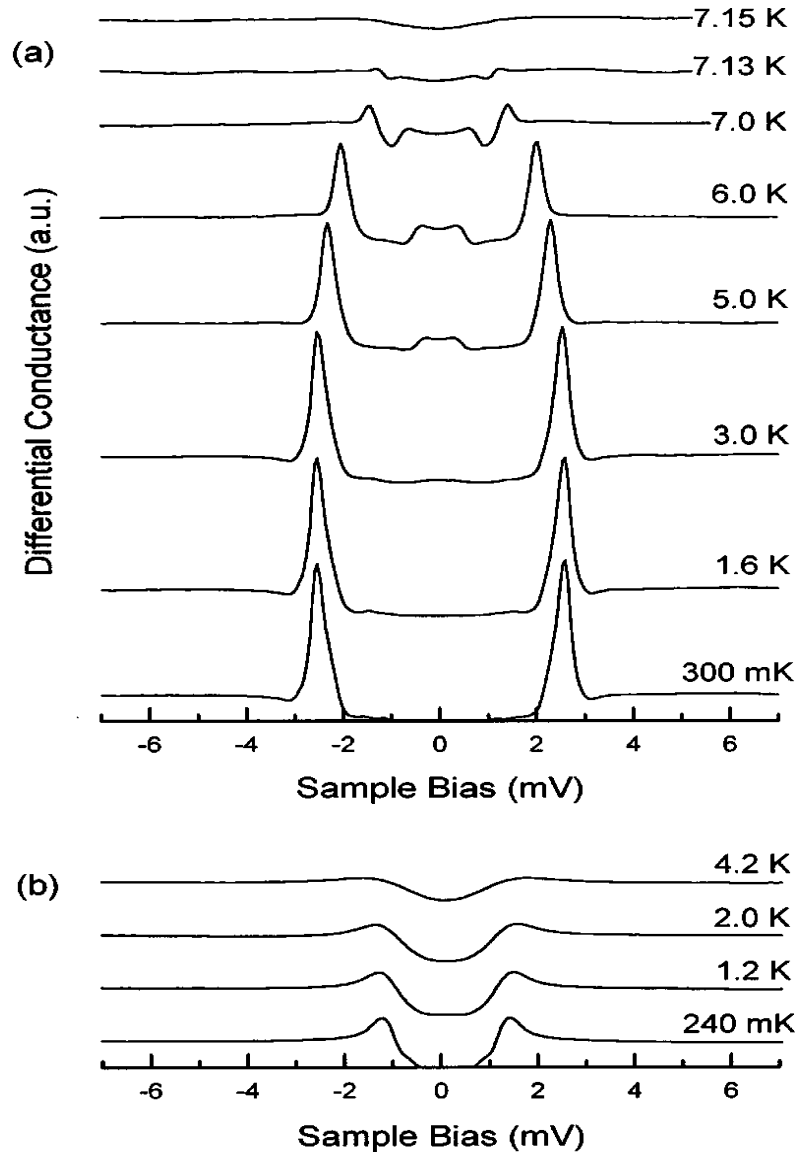


Figure 3. (a) Measured differential conductance spectra for tunneling (SS) between a superconducting Nb tip and a NbSe₂ surface. (b) Measured differential conductance spectra for tunneling (NS) between a PtIr tip and a NbSe₂ surface. Comparison between the SS and NS tunneling spectra, plotted on the same scale, shows the dramatic enhancement in sharpness of the features obtained with a superconducting tip. (Pan et al., 1998)

possible materials in order to find higher T_c superconductors. Y-Ba-Cu-O was found with a $T_c = 93K$ in 1987 [36], BiSrCaCu₂O_x was found with a T_c above $105K$ in 1988 [37], bulk superconductivity at $120K$ in the Tl-Ca/Ba-Cu-O system was found in 1988 [38], and in 1993 HgBa₂Ca₂Cu₃O_{8+δ} was found with a transition temperature $T_c > 135K$ and that T_c reached $150K$ under a high pressure ($150kbar$) [39]. During the past three years, superconductivity research has achieved great improvements; October 2009 superconductors.org herein reported the observation of a world record transition temperature near $254K$ with (Tl₄Ba)Ba₂Ca₂Cu₇O₁₃₊. With such a high critical temperature T_c this becomes the first material to enter a superconductive state at temperatures commonly found in household freezers.

CHAPTER II

EXPERIMENTAL APPARATUS

A. Fiber Optic Interferometer

We used a homemade fiber optic interferometer to test and measure the step size of the piezoceramic stacks and the coarse approach walker system. The schematic of the fiber optic interferometer system is illustrated in Figure 4. The laser light is generated by a Melles Griot diode laser with a wavelength of 6419 \AA . A fiber port alignment (OFR PAF-X-11-633) is used to focus the laser light into a single mode fiber that is connected to a 2x2 fiber optic directional coupler (Newport N31628). The coupler splits the input beam (port A) into two output beams with a ratio of 50:50 (ports B and C). The output of port C is used to monitor the amplitude of the laser. Port B is connected to another single mode fiber that is placed in close proximity ($\sim 1mm$) to a reflecting surface attached to the object whose motion is to be measured. Some light is reflected back into the fiber from the surface at the end of the fiber. The light that leaves the fiber is reflected by the moving reflecting surface and reenters the same fiber. Both beams are directed by the coupler to port D where the interference between the two beams is detected by a photo detector (Thorlabs PDA55).

The laser lights reflected from the end of the fiber and the moving reflecting surface can be expressed as $P_1 = A_1 e^{i\phi_1}$ and $P_2 = A_2 e^{i\phi_2}$; where A_1 and A_2 are the

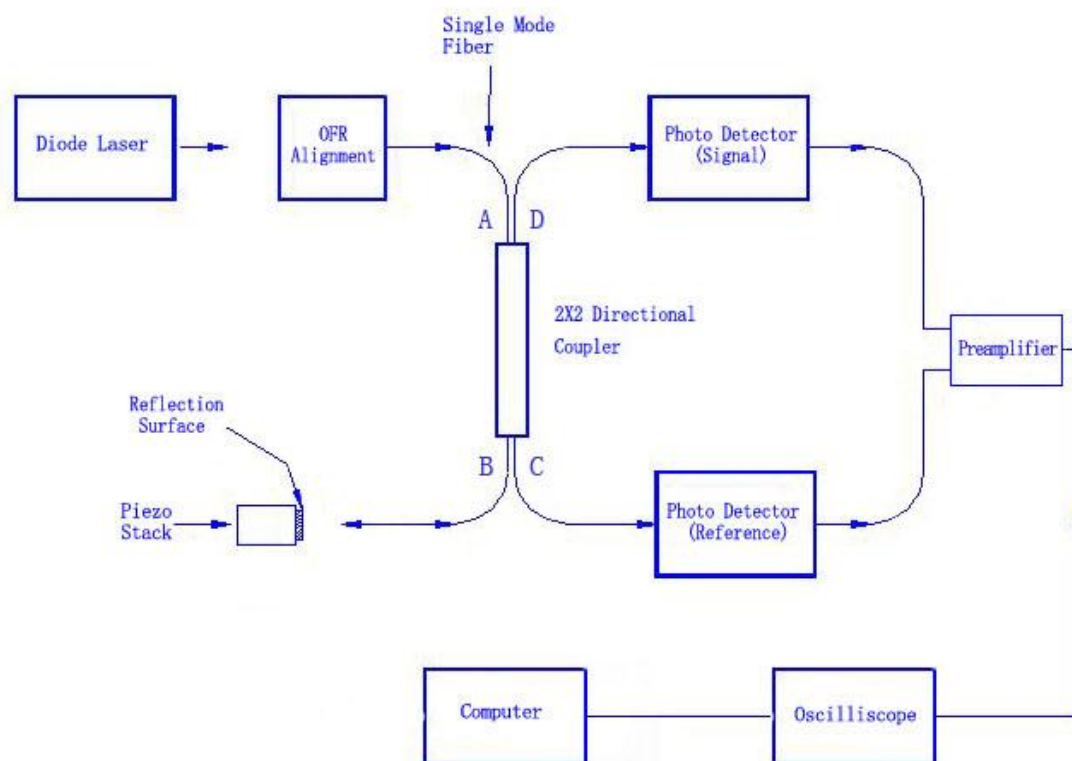


Figure 4. Schematic of the fiber optic interferometer.

amplitudes and ϕ_1 and ϕ_2 are the absolute phase angles (the time dependence terms are not shown). The total amplitude signal seen by the detector is therefore,

$$P = A_1 e^{i\phi_1} + A_2 e^{i\phi_2} = e^{i\phi_1} (A_1 + A_2 e^{i(\phi_2 - \phi_1)}) \quad (2.1)$$

with the corresponding intensity,

$$I = P \cdot P^* = A_1^2 + A_2^2 + A_1 A_2 (e^{i(\phi_2 - \phi_1)} + e^{-i(\phi_2 - \phi_1)}) = A_1^2 + A_2^2 + 2A_1 A_2 \cos(\phi_2 - \phi_1) \quad (2.2)$$

The phase difference $\Delta\phi = \phi_2 - \phi_1$ is simply related to the difference in the length traveled by the two beams, $\Delta\phi = 2\pi \frac{2d}{\lambda} = \frac{4\pi d}{\lambda}$.

The PDA55 converts this intensity to a voltage signal. A low noise preamplifier (ITHACO 1201) amplifies the interference voltage signal with a gain of 20~100. Both the amplified signal and the voltages on the piezoceramic stacks are recorded by a digital oscilloscope (LeCroy 9450). A Labview program (Measure_Interference.vi) is used to remotely control the oscilloscope to display the interference signal versus the piezoceramic voltages. To measure the displacement, the piezoceramic voltage is swept with a low frequency 10Hz sine wave with a typically voltage amplitude of 140V.

Samples of the signal are shown in Figure 5. Figure 5a shows the raw signals and Figure 5b shows the resulting Lissajous figure. The minimum and maximum peaks correspond to voltages for which the phase difference is either 0 or π . Consequently, one can calculate the distance traveled for this voltage difference ΔV or equivalently the displacement-voltage coefficient of the piezoceramic stacks,

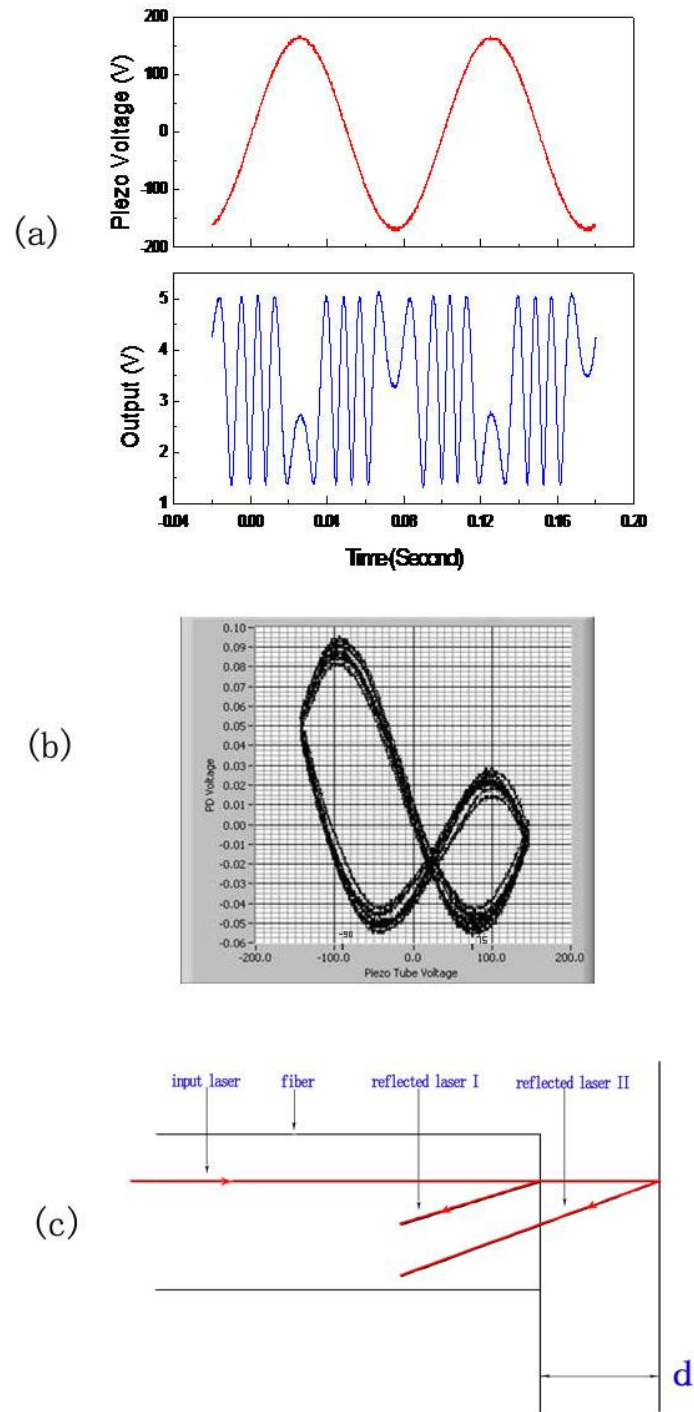


Figure 5. Working principle of the fiber optic interferometer. (a) The voltage applied on the piezoceramic stack and the reflected PD voltage. (b) The PD voltage versus piezoceramic voltage graph. (c) Illustration of the two reflected beams at the end of the fiber.

$$\delta = \frac{d}{\Delta V} = \frac{\pi \cdot \lambda}{4\pi \cdot \Delta V} = \frac{\lambda}{4\Delta V} \quad (2.3)$$

where $\lambda = 6419 \text{ \AA}$. Using this method, the displacement-voltage coefficients of the six piezoceramic stacks are, $\delta_1 = \delta_2 = \delta_3 = 14.6 \text{ \AA/V}$, and $\delta_4 = \delta_5 = \delta_6 = 15.3 \text{ \AA/V}$.

B. STM Head

The scanning tunneling microscope (STM) has revolutionized the surface science by providing a method to directly obtain atomic scale images and electronic structures of various samples. In order to improve the stability of the microscope and reduce electronic and thermal noise, a variety of low temperature ultrahigh vacuum (UHV) STM designs have been developed. After studying and comparing the advantages of these designs, we chose to build our low temperature STM incorporating features of the STMs of W. Ho et al. [40] and S. H. Pan [6].

Operating a STM at low temperatures brings advantages such as low thermal drift and reduced mobility of absorbed atoms and molecules, both of which are required for atomic resolution measurements. In addition, the thermal broadening of the Fermi surface is also reduced. However, most cryostats have some mechanical vibrations which can often degrade atomic resolution measurements. We used four principal methods to reduce the effects of these vibrations: (1) a very rigid STM head that is less susceptible to vibrations, (2) a rigid ^3He cryostat design that has a large and massive ^4He pot that can be pumped in a one-shot mode to avoid vibration noise from a continuous

fill line, (3) the entire cryostat is floated on a low frequency air vibration-isolation frame to reduce the transmission of vibrations coming from the floor, (4) the cryostat support structure is within a shielded room that sits on springs buried in the sub-floor, so that the cryostat is further isolated from the vibrations coming from the building.

Figure 6 shows a drawing of our STM head. It was designed to be as compact as possible to make it less susceptible to vibrations. It measures $1.4in$ in diameter by $2.2in$ in height. All the materials were chosen to be compatible with operation in an ultra high vacuum (UHV). Our STM head integrates a conventional four-quadrant piezoceramic tube scanner (13) and a coarse approach piezoceramic walker into the main body (6). The main body was machined from a single piece of titanium that shields the inner tip from electronic noise due to external sources. In addition, the thermal expansion of titanium is a good match to the thermal expansion of the piezoceramic tubes and Macor [41, 42] and therefore reduces the relative motion of the tip when the temperature of the STM is changed. The top part is a spring loaded sample plate receptacle (1) also machined from titanium that makes good electronic and thermal contact to the molybdenum sample plate (2) and thereby to the sample that is loaded on the bottom of the sample plate. Between the titanium body and sample holder receptacle there is a Macor insulator (8). This electrically isolates the sample from the body of the STM. The approach piezoceramic walker [43] consists of the main body (6), a sapphire

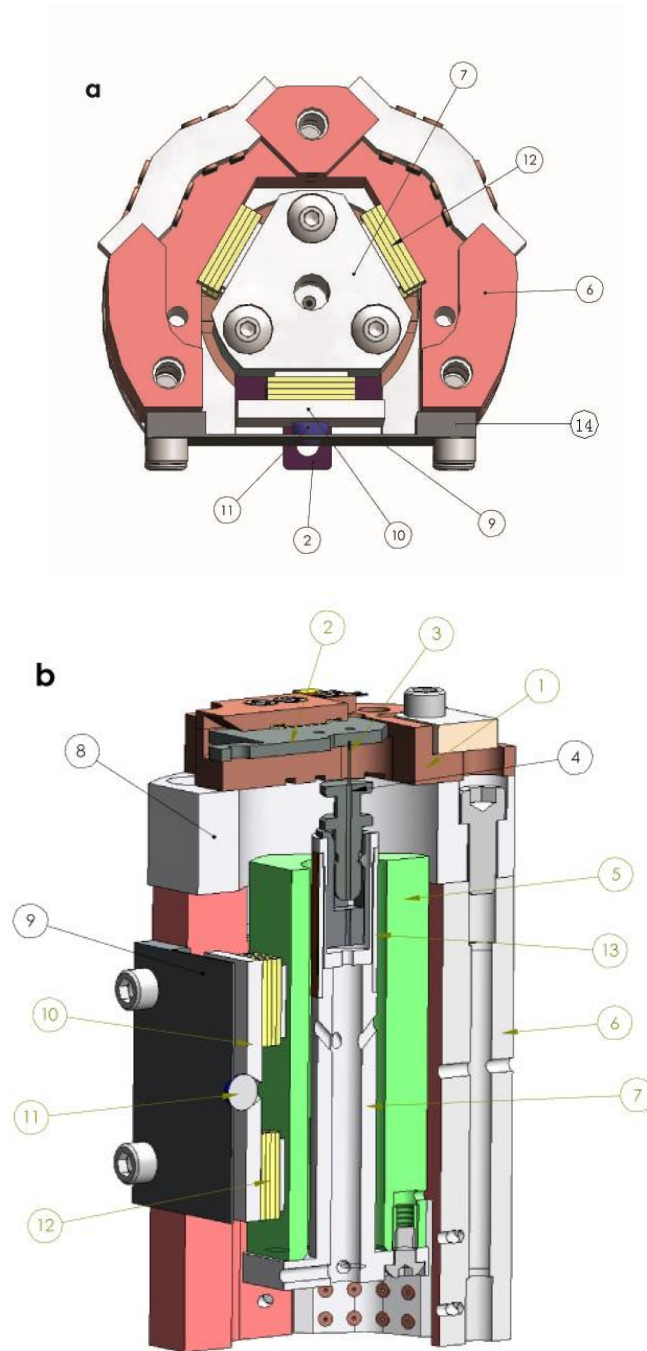


Figure 6. STM head. (a) Bottom view. (b) Side view (1.4 *in* in diameter by 2.2 *in* in height). (1) Sample receptacle. (2) Molybdenum sample plate. (3) Tip. (4) Tip holder. (5) Sapphire prism. (6) Titanium body. (7) Tube holder. (8) Macor insulator. (9) BeCu spring plate. (10) Al_2O_3 plate. (11) Sapphire ball. (12) Shear piezoceramic stack. (13) Piezoceramic tube scanner. (14) Spacer.

prism (5) with a central hole, six shear piezoceramic stacks (12) with thin Al_2O_3 plates on the surfaces that contact the prism, a BeCu spring press plate (9), and two spacers (14). The sapphire prism is clamped between the six piezoceramic stacks (PZT-8) [44] with the force established by the BeCu spring plate that presses the front two piezoceramic stacks onto the sapphire prism via a 3mm diameter sapphire ball. The piezoceramic tube scanner (13) (PZT-4) [44], 0.25in in diameter by 0.4in in length, is mounted on the Macor tube holder (7) and is fixed in the center of the sapphire prism. There are five electrodes on the gold coated piezoceramic tube scanner: four quadrants on the outer surface and one on the inner. With an applied voltage of $\pm 130\text{V}$, the maximum x and y scan range is $2\mu\text{m} \times 2\mu\text{m}$ and the maximum z scan range is about 600nm . The STM tip (3) is usually made from a thin Pt80/Ir20 wire (0.008in in diameter) that is sharpened by electrochemical etching [45, 46]. The chemical etching solution consists of 14g of $\text{CrCl}_2 \cdot 2\text{H}_2\text{O}$ powder in 40ml water and 40ml acetone. The tip is inserted and fixed via friction into the tip holder (4) mounted on the top of tube scanner. A Cooner coaxial cable with a superconducting inner conductor is used to connect the tip with the outside control box SPM 1000 in order to reduce the electronic pick up noise.

The coarse approach piezo walker was invented by S. H. Pan in 1993 [43] and has successfully been used in low temperature scanning probe microscopes around the

world [11, 14, 47]. It has six piezoceramic stacks; each piezoceramic stack is made of four shear mode piezoceramic plates (PZT-8) [44], that are $0.3in \times 0.3in$ in size and $0.02in$ in thickness. The schematic of the piezoceramic stack and its working principle are illustrated in Figure 7. Starting with a square plate, each plate is shaped using sand paper as indicated in Figure 7e and then epoxied with a UHV compatible, electrically conducting epoxy H21D [48] so that adjoining plates have the opposite orientations and therefore can share a common high voltage electrode as showed in Figure 7e. In order to ensure that the plates are kept parallel as the epoxy cures, each pair of plates is assembled in a Precision Parallel Screwless Vise [49] that can clamp the plates together with a uniform pressure on the plates' surfaces. The Precision Parallel Screwless Vise was also used in later gluing steps to ensure that all of the plates remain parallel to each other. A high power lamp (250 W) was used to heat the plates and epoxy to about $400K$ so that the epoxy would cure in 20 minutes. Finally, six small Al_2O_3 plates ($0.2in \times 0.2in \times 0.2in$) are glued on the top of each piezoceramic stack.

When a voltage is applied to the piezoceramic stack shown in Figure 7c, all four piezoceramic plates shear in the same direction, so that the total shear displacement is four times that of a single plate. A fiber optic interferometer is used to measure the unit displacement of the piezoceramic stack; which is around 15 \AA per volt. Each pair of

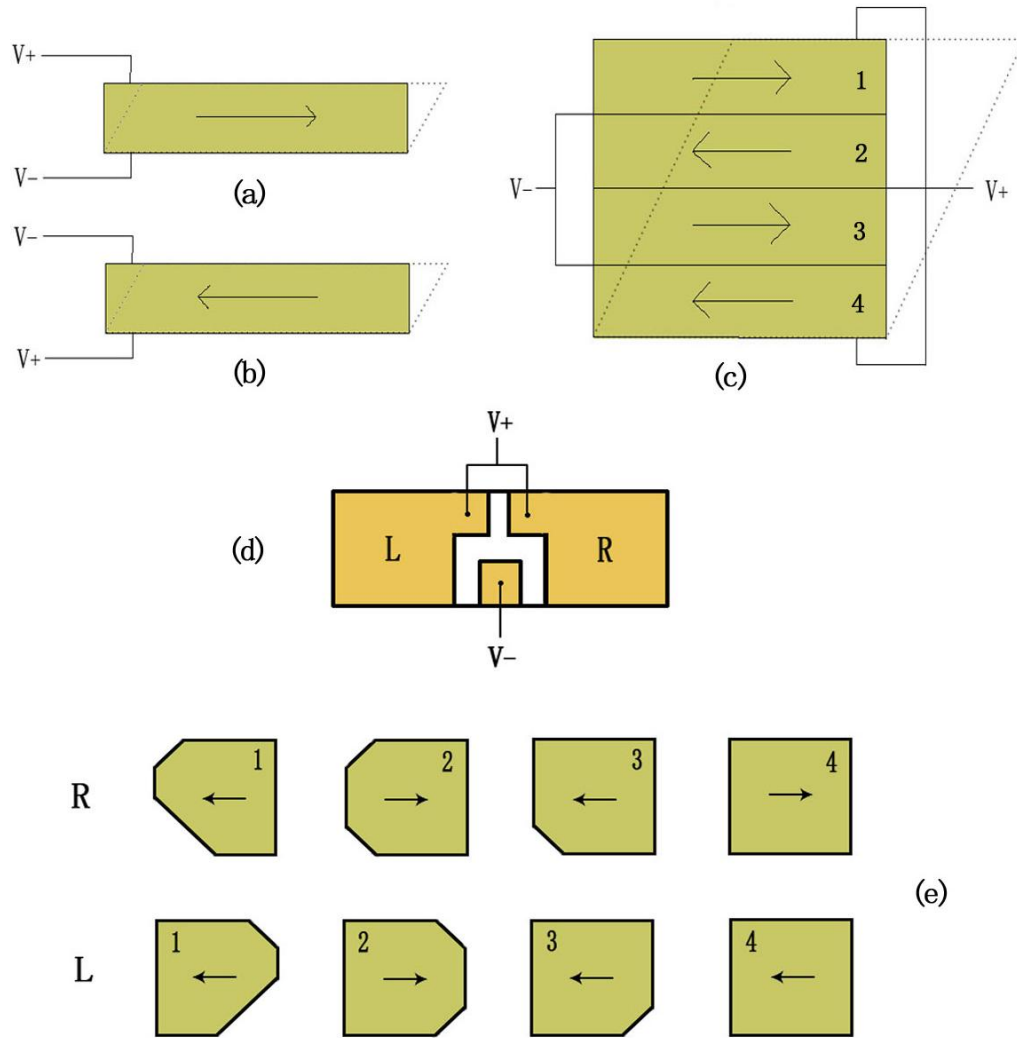


Figure 7. Schematic of working principle of the piezoceramic stacks. (a) The shear orientation of the piezoceramic stack is to the right; as a positive voltage is applied on the top surface of the plate, the plate shifts to the right (dashed line). (b) The shear orientation of the piezoceramic stack is to the left; as a positive voltage is applied on the bottom surface of the plate, the plate still shifts to the right (dashed line). (c) Four piezoceramic plates are epoxied together in the manner shown; as a positive voltage is applied on the top surface of the stack, the stack shifts to the right (dashed line) with four times displacement of a single plate. (d) Al_2O_3 bottom plate deposited with $\sim 100\text{nm}$ gold film. (e) Shape of each piezoceramic plate in piezo stack. Black arrows indicate the shear orientations of the piezoceramic plate; V_+ and V_- indicate the positive and negative voltages applied on the plates; numbers indicate the layers of the stacks.

piezoceramic stack is epoxied to an Al_2O_3 plate ($0.3\text{in} \times 0.8\text{in}$ and 0.02in in thickness) that serves as a junction point for the high voltage leads. The voltage pad configuration consists of a 100nm gold film as shown in Figure 7d.

The working principle of the coarse approach piezoceramic walker is illustrated in Figure 8; for clarity, only four of the piezoceramic stacks are shown. The piezoceramic stacks hold the prism in place by frictional forces. When a voltage of 240V is quickly applied to one piezoceramic stack, it undergoes a shear strain and slides backwards on the surface of the prism (to the right). The prism does not move because the frictional force from the other stacks is larger than that from this moving stack (shown in Figure 8a). After a short delay ($200\mu\text{s}$), the same voltage is applied to the second piezoceramic stack, and as before, the second stack will slide backward (to the right). The same procedure is applied to each stack one by one. After all of the stacks have slid backwards, all of the voltages applied to the stacks are then reduced to zero at the same time. The stacks now remain fixed to the prism and the prism is carried forward by one step (to the left) (shown in Figure 8a(5)). This design has some advantages. Because the walker does not rely on inertia, it can work in the vertical direction with only a small change in the step-size due to gravity. In addition, the piezoceramic stacks constantly hold the prism and therefore no voltage is required to keep the prism in position when it is stationary. These features make the whole STM stable and rigid, and

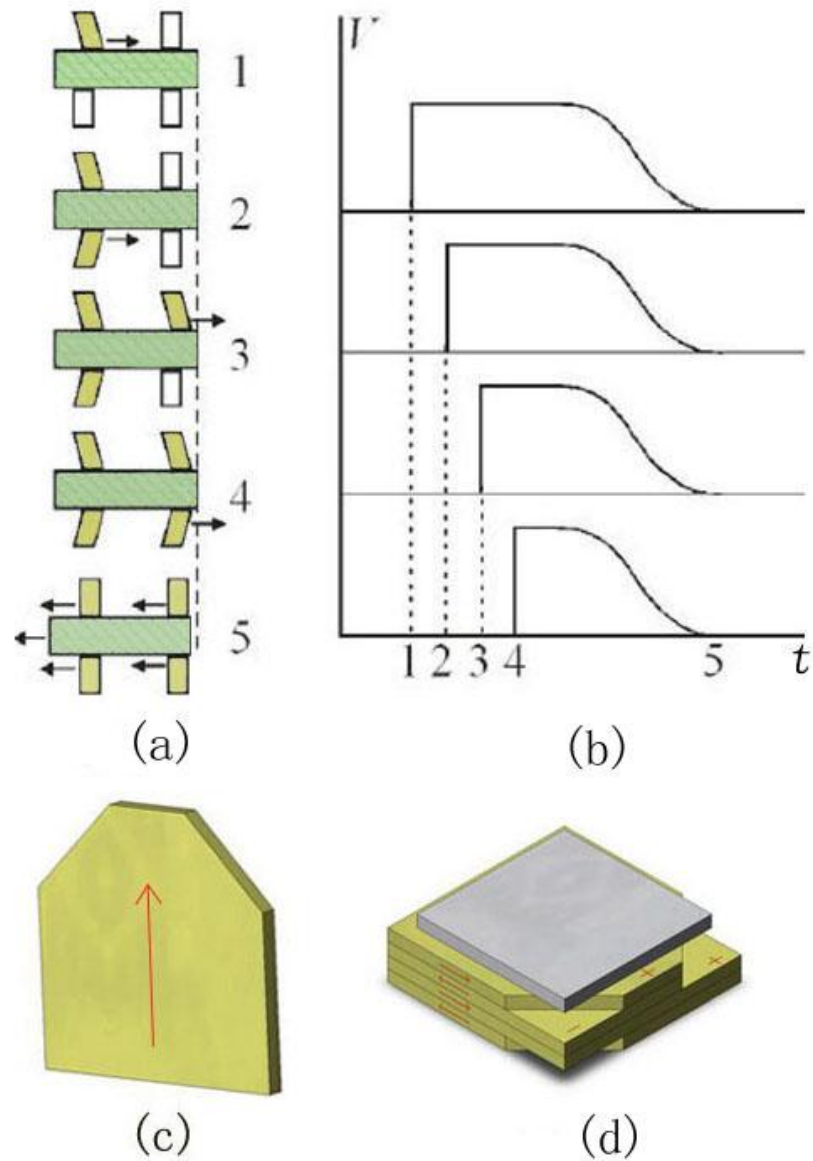


Figure 8, Schematic illustration of the working principle of the coarse approach piezoceramic walker. (a) The sequence of motions of the shear piezoceramic stacks and sapphire prism. (b) The sequence of voltages applied to each piezoceramic stack to produce the motions in (a). (c) Single shear piezoceramic plate. (d) Shear piezoceramic stack with a thin Al_2O_3 plate on the top. Red arrows indicate the shear directions of the plates and “ \pm ” indicate the positive and negative voltage applied on the plate. ((a) and (b), Pan et al., 1999).

reduce any displacement noise from the coarse approach walker.

The thickness of the spacers, between the BeCu spring plate and titanium body (shown in Figure 6a), determines the bending of the spring plate, and thereby the clamping force established by the spring plate. If the clamping force is within a specific range, the stepsize of the piezoceramic walker is almost independent of the force. If the clamping force is above or below this range, the stepsize decreases because too large of a force prevents the piezoceramic stacks from sliding on the prism and too small of a force prevents the piezoceramic stacks from grabbing the sapphire prism. As the STM is cooled, the sapphire prism shrinks less than the titanium body [41, 42], causing the clamping force to increase. Therefore, one cannot use spacers that are too thin because this would result in a clamping force that is too large and therefore a very small stepsize. Normally, a 0.085 or 0.090 *in* spacer is used on our STM. With these spacers, the BeCu spring plate does not provide enough clamping force at room temperature to compensate for the weight of the center part of the piezoceramic walker (prism and the scanning parts) and therefore the upward steps are smaller than the downward ones. The room temperature stepsizes of the piezoceramic walker are shown in Table I. We also see that the upward stepsizes with the 0.085 *in* spacers are larger than those with the 0.090 *in* spacers and the downward stepsizes with 0.085 *in* spacers are smaller than ones with the 0.090 *in* spacers. This is consistent because the piezoceramic walker with the

0.090in spacers is more loose than that with the 0.085in spacers, and therefore it is harder to move the prism upwards and easier to move it downwards due to gravity. As indicated in Table I, the room temperature measured stepsizes are much smaller than the calculated ones (determined from the measured unit displacements of the piezoceramic stacks and the applied voltages). One possible explanation is that the piezoceramic stacks may not perfectly be parallel to the prism surface and therefore the small Al_2O_3 plates on the top off the piezoceramic stacks (shown in Figure 8d) may not entirely contact the prism surface. Therefore the friction forces between the prism and the individual piezoceramic stacks may be different causing some of the piezoceramic stacks not to work as well as the others.

Table I. Room Temperature Stepsizes of the Piezoceramic Walker

Voltage on Stacks	120V	180V	240V
Measured Stepsize with 0.085 inch Spacers on the STM			
Up	353 Å/step	805 Å/step	1212 Å/step
Down	427 Å/step	1041 Å/step	1489 Å/step
Measured Stepsize with 0.090 inch Spacers on the STM			
Up	305 Å/step	763 Å/step	1083 Å/step
Down	565 Å/step	1180 Å/step	1430 Å/step
Calculated Stepsize			
Up & Down	1800 Å/step	2400 Å/step	3600 Å/step

One can adjust the stepsize of the piezoceramic walker by adjusting the thickness of the spacers and the piezoceramic stacks' driving voltage. The stepsize of the piezoceramic walker will decrease when the temperature decreases due to the properties

of piezoceramic materials and the effects of thermal contraction. The measured ratio of the stepsizes at room, liquid nitrogen, and liquid helium temperature is:

$$\text{Room} : \text{LN}_2 : \text{LHe} = 4.94 : 2.04 : 1.$$

C. ^3He Cryostat

To test the behavior of the STM, a homemade ^3He cryostat was chosen for the low temperature platform. Because of the difference in mass, the vapor pressures of ^3He and ^4He liquids are quite different; at 1.2 K the vapor pressure of ^3He is approximately 75 times greater than that of ^4He . Therefore a pumped bath of liquid ^4He can reach a temperature of approximately 1.2 K , whereas liquid ^3He can be pumped down to about 0.3 K [50]. The cryostat was originally built by Robert Burns and Mark Wainwright over the years 1988-1990. It has several key features that make it possible to easily adapt it for use in a variety of experiments.

One feature is the extensive vibration isolation system which supports the entire apparatus. Figure 9 shows the schematic of our ^3He cryostat; only two support legs are shown for simplicity. The room temperature flange of the cryostat sits on a brass annulus that has feedthroughs with which one can access the Dewar space. The annulus sits on a hexagonal aluminum plate that is mounted to a triangular structure made from box aluminum that has been backfilled with lead shot (approximately 700 lbs). This triangular structure is supported by three TMC low frequency pneumatic isolators. The

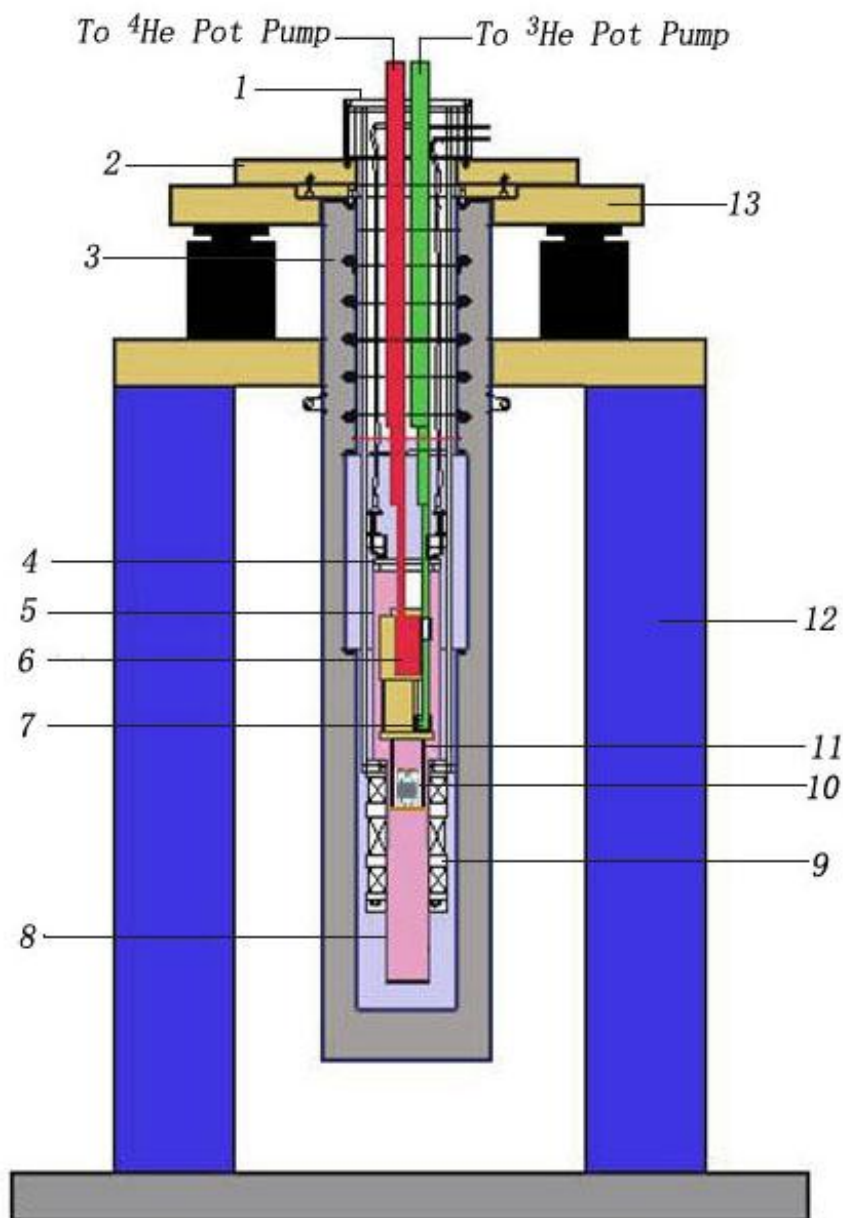


Figure 9. Schematic of homemade ^3He cryostat. (1) Room temperature flange. (2) Room temperature plate. (3) Dewar. (4) 4 K flange. (5) Vacuum can. (6) ^4He pot. (7) ^3He pot. (8) Vacuum can tail. (9) Superconducting magnet. (10) STM head. (11) Spring. (12) Supporting leg. (13) Table top of the vibration isolation table.

pneumatic isolators are supported by an aluminum tripod that is approximately 88in tall and 82in on each side. When the three pneumatic isolators are inflated with high pressure nitrogen gas ($\sim 75\text{ psi}$), the entire cryostat is floated and isolated from the vibrations coming from the floor. Additionally, all pumping lines and tubes connected to the top of the cryostat are isolated from the vibrations of the mechanical pumps by double gimbal mounts and flexible tubing. Finally, the room itself in which the cryostat resides sits on springs buried in the sub-floor, so that the cryostat is further isolated from the vibrations coming from the building. The whole room is also shielded by copper walls to reduce unwanted electromagnetic noise. All of these safeguards help to ensure that any experiment performed with this cryostat is free from electronic and vibration noise which is especially crucial for maintaining stability in the tunnel junctions.

The cryostat consists of several stages, denoted by the ultimate temperature that each stage reaches during operation. The uppermost section of the cryostat is in contact with the atmosphere at room temperature, and thus is normally at 295 K . All pumping lines enter the top of the cryostat at the Room Temperature Flange (1) and are sealed with polymer O-ring, quick-connect fittings. All electrical connections to the exterior of the cryostat such as the bath thermometer and heaters go through hermetically sealed multi-pin connectors mounted on the eight-sided annulus. Similarly, the wires and cables for the inside of the cryostat go through hermetically sealed multi-pin connectors or

hermetically sealed Microdot connectors mounted to ports at the top of the cryostat. In the cryostat, electrical lines for thermometers and heaters are typically manganin wires ($\sim 90\text{ Ohms}$). All other signal lines are Cooner coaxial cables with either a stainless steel or superconductor inner conductor.

The Dewar (3) is just below the Room Temperature Plate (2). It is a large aluminum-clad fiberglass cylinder weighing about 350 lbs . The Dewar is raised up from the trench below the shielded room by a 1.3 hp variable-speed power winch. It is bolted to the underside of the Room Temperature Plate, and sealed with a polymer O-ring. The vacuum can (5) and vacuum can tail (8) are inside the Dewar. Using a combination of mechanical rotary pumps and an oil diffusion pump (that is in the Leak Detector), we can easily reach a vacuum pressure of $<10^{-5}\text{ Torr}$ inside the vacuum can at room temperature. There are six Radiation Baffles between the Room Temperature Plate and 4 K flange (4) in order to conserve the liquid helium in the bath by reducing the thermal radiation from room temperature to the lower parts of the cryostat.

The Scanning Tunneling Microscope head (10), ^4He pot (6), and ^3He pot (7) are inside the vacuum can. The 4 K flange is sealed to the can by fuse wire (0.025 in in diameter) O-ring [51], one cannot use polymer O-rings, because at liquid helium temperature and below, most pliable polymers become brittle and no longer seal effectively. After the cryostat is cooled down, the 4 K flange is usually immersed in the

liquid helium; and almost everything that enters the can (capillaries, electrical leads) is anchored to the 4 K flange in order to intercept the heat conducted from above.

The ^4He pot is just below the 4 K flange. It consists of a large block of Oxygen Free High Conductivity (OFHC) copper into which a cylindrical chamber with an internal volume of 56.5 in^3 has been machined. To fill the ^4He pot, two copper-nickel capillaries connect the ^4He pot to the liquid helium bath in the Dewar. One fill capillary has a slightly larger impedance than the other, providing two rates of flow into the ^4He pot. The larger impedance capillary can be used to continuously fill the ^4He pot. Unfortunately, a continuous fill line often produces vibration noise due to “whistling” of the liquid helium in the fill capillary as it enters the ^4He pot. To avoid this, one can one-shot the pot by quickly filling it with the smaller impedance capillary. In this way both fill lines can be closed while pumping on the ^4He pot. Each capillary can be opened or closed by pneumatically controlled valves in the bath. These valves are controlled by the four fast/slow pressure ($> 40\text{ psi}$) and fast/slow vacuum (1 Torr) valves that are on the top of the vibration-isolation table top (13). A large mechanical pump (^4He pump) is used to pump on the liquid helium in the ^4He pot

Below the ^4He pot is the ^3He Pot which is constructed of OFHC copper with an internal volume of 0.57 in^3 . The ^3He Pot rests on the ^3He stage and is connected to the underside of the ^4He pot by hollow stainless steel tubes. Because stainless steel is a poor

conductor of heat, the ^3He Pot is thermally isolated from the rest of the cryostat. Therefore when the sample is heated, the ^3He Pot can be heated to a relatively high temperature (tens of Kelvin), while the temperature of the ^4He pot is not greatly affected. For example, when the ^3He pot reaches around 30 K , the ^4He pot is just around 10 K .

Because ^3He gas is very expensive, it is circulated within a closed system. Initially the ^3He gas is condensed into a liquid by the ^4He pot and then fills the ^3He pot by a capillary. It is then evaporated by a large mechanical pump (^3He pump) and roots blower, cooling the ^3He pot and lower stages to 0.3 K . The exhaust of these pumps (which is still ^3He gas) is then purified through a series of 77 K and 4 K traps, and forced back into the cryostat to repeat the cycle.

The STM head is firmly mounted upside down underneath the ^3He pot stage through a round OFHC copper plate, which helps to form a strong thermal link between the STM head and the ^3He pot stage, so that the STM head can be cooled by the ^3He pot quickly. In a future design, the STM head can be suspended by three springs (11) beneath the ^3He pot stage in order to further reduce the vibration coming from the cryostat. In this configuration the STM will be cooled by a flexible OFHC copper braid. All the cables and connections to the STM head are thermally anchored to both the ^4He and ^3He pots in order to reduce the heat transferred from the warmer sections of the cryostat. A small heater is mounted on the sample stage of the STM head. By applying

100mA current (40V) across it, this heater can heat the sample to room temperature in order to clean the sample surface while the rest of the cryostat remains at low temperatures.

Lastly, the STM head is surrounded by an extension to the vacuum can, the vacuum can tail (8). The tail is designed to fit within the bore of an eight Tesla NbTi Superconducting Magnet (9). The magnet has an inner bore of 3.5in, an overall length of 12.6in, and requires 75A of current to reach full field strength (8T). It is equipped with a built-in superconducting switch and switch heater that enables it to run in a persistent current mode. However, due to an internal weak link, the magnet cannot be run in persistent current mode at the present time.

D. Electrical Wiring

On the cryostat, there are two ports that house the hermitically sealed Microdot coaxial connectors; one has only two connectors and is used for the tip wire. It was added later to accommodate a new coax with a lower capacitance in order to reduce the noise in the current preamp (stainless steel braid outer conductor, inner conductor of NiMoTi with a Teflon insulation, and 120 pF in capacitance). The second port has 19-pin and is used for the high voltage lines to the stacks and the tube scanner. Cooner coaxial cables (stainless steel braid outer conductor, inner conductor of NbTi with a Teflon insulation, and 260 pF in capacitance.) run continuously from these room

temperature connectors to a bank of Microdot connectors mounted on the outside of the ^4He pot. Each cable is thermally anchored at the 4 K flange and at the ^4He Pot. Figure 10 shows the assembly for all these connections. The devices and signal lines from the STM that attach to this bank are detailed in Table II.

A 20-pin connector is mounted on the bottom of the titanium body of the STM in order to connect these coaxial cables from the Microdot connector banks with the Kapton insulated copper wires which are directly glued to the piezoceramic stacks and the tube scanner. There are two types of Kapton insulated copper wires with different diameters; nine thicker ones with 0.008 in in diameter are for the piezoceramic stacks that have a typical working voltage of 240 V ; five thinner ones, 0.0035 in in diameter, are for the scan tube that operate at voltages less than 130 V . Figure 11 shows this 20-pin connector. The connections are described in Table III.

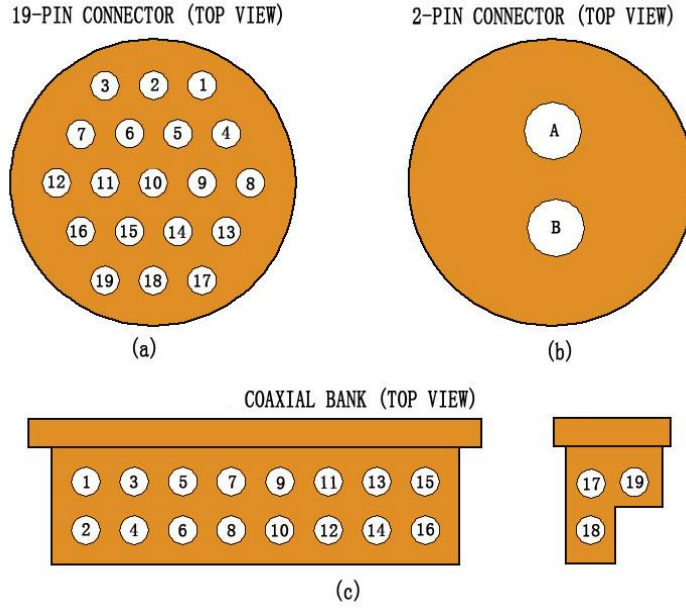


Figure 10. Multi-pin coaxial connectors and banks.

Table II. Shielded Wiring to Two Multi-Pin Connectors

Coax Cable Number	Pin Number	Resistance (Ω)	Device/Function
1	1	89.1	Open
2	2	88.6	Open
3	3	89.3	Inner surface of scan tube
4	4	89.4	Outer surface pair I of scan tube
5	5	89.3	Outer surface pair I of scan tube
6	6	89.3	Outer surface pair II of scan tube
7	7	89.5	Outer surface pair II of scan tube
8	8	89.2	Piezoceramic stack I
9	9	89.1	Piezoceramic stack II
10	10	89.4	Piezoceramic stack III
11	11	89.3	Piezoceramic stack IV
12	12	89.4	Ground for all six piezo stacks
13	13	89.5	Piezoceramic stack V
14	14	89.3	Piezoceramic stack VI
15	15	89.3	Bias (to the sample plate)
16	16	89.8	Open
17	17	89.5	^4He pot capacitive level gauge
18	18	89.3	^4He pot capacitive level gauge
19	19	89.5	Open
A	A	87.3	Scanning Tip
B	B	N/A	Open

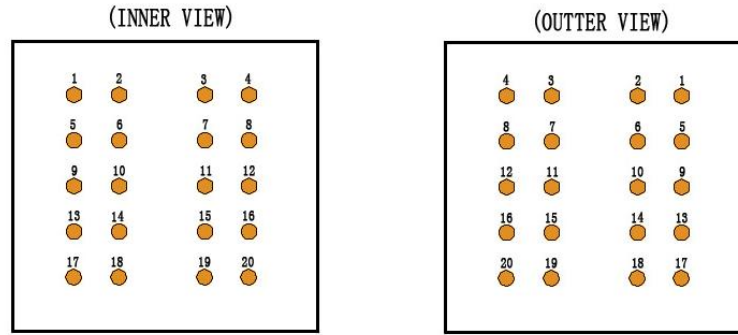


Figure 11. Inner and outer view of the 20-pin connector that connects the piezo stacks and the scan tube with the coaxial cables and is mounted on the bottom of STM head.

Table III. Wiring to a 20-Pin Connector on the STM Head

Pin #	Device/Fuction	Pin #	Device/Fuction
1	Piezoceramic stack I	11	Open
2	Piezoceramic stack II	12	Ground for stack pair III
3	Piezoceramic stack III	13	Open
4	Piezoceramic stack IV	14	Inner surface of scan tube
5	Open	15	Open
6	Open	16	Piezoceramic stack V
7	Ground for stack pair I	17	Outer surface pair II of scan tube
8	Ground for stack pair II	18	Outer surface pair II of scan tube
9	Outer surface pair I of scan tube	19	Open
10	Outer surface pair I of scan tube	20	Piezoceramic stack VI

CHAPTER III

EXPERIMENTAL PROCEDURES

A. Preparation of the STM Head at Room Temperature

First, check all the wiring of the STM head to make sure that the electrodes of the center scanning tube and all of the piezoceramic stacks make good electrical connections to the 20-pin connector (shown in Figure 11). Check the alignment of the top pair of the piezoceramic stacks, which is pressed by the BeCu spring plate, and make sure the screws that fix the BeCu spring plate are firmly tightened. Then mount the STM head upside down underneath the ^3He stage of the cryostat through a round OFHC copper plate and check that the STM head makes good electrical connections to all of the controlling and measuring electronics (shown in Figure 12).

Next, install a sharp tip and the Standard Calibration sample into the STM head. Turn on the coarse approach control box and the RHK SPM 100 data acquisition box. At this point, there should be a bias voltage applied between the tip and the sample. Use a voltmeter to check that this voltage has the correct value. Then start the approach subroutine to move the tip to the “in range” position to check that the piezoceramic walker system is working.

After the tip arrives at the “in range” position, scan the Standard Calibration sample to see whether the tip is sharp enough and the STM works well. At this time, one can verify that the calibration settings in the SPM 100 control software SPM 32 give the correct x and y displacements. One can also make measurements of the current-bias

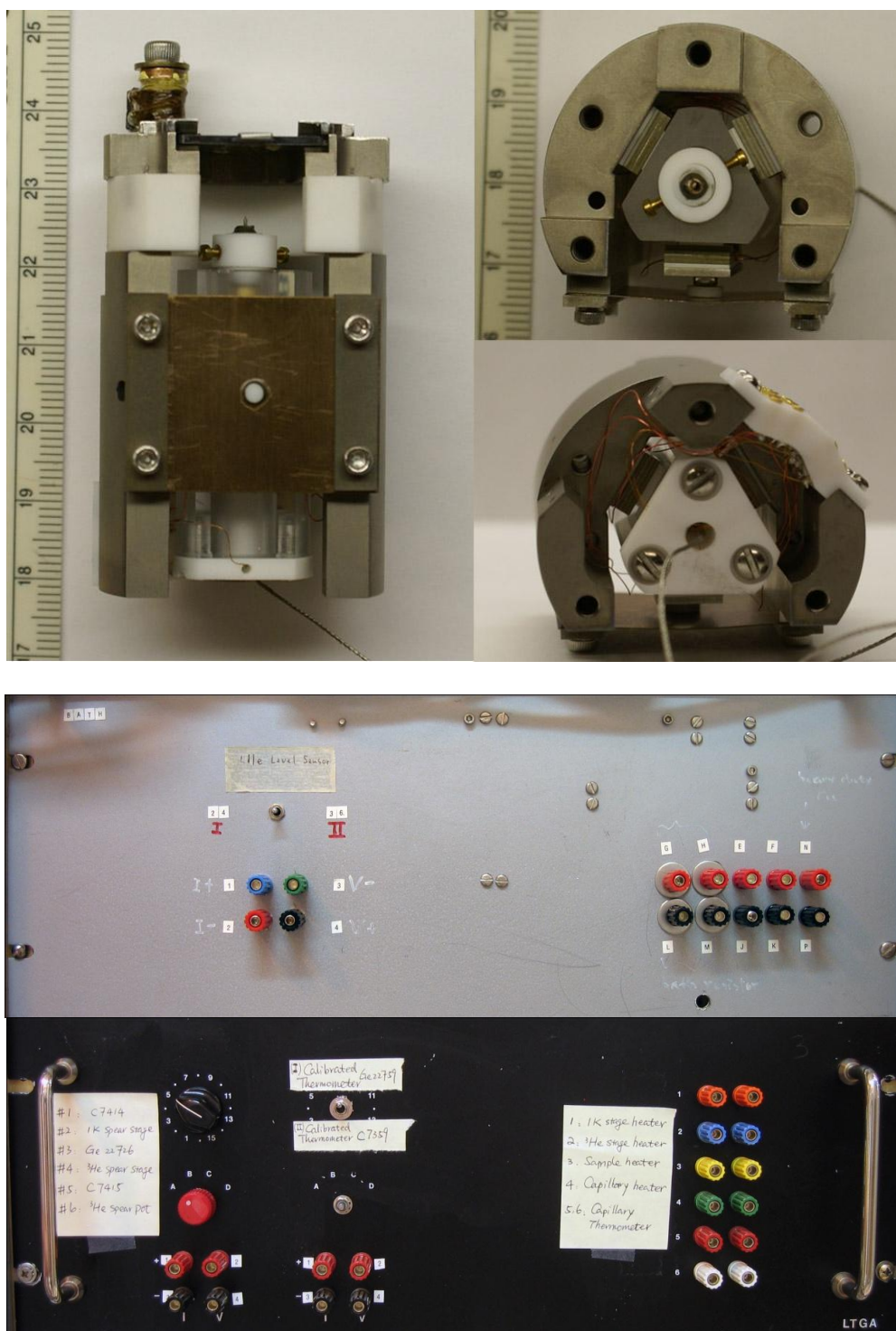


Figure 12. Photographs of the top and bottom details of the STM (scale in centimeters) and photograph of the control panels for all thermometers and heaters.

voltage and differential conductance-bias voltage curves to verify that all the proper connections have been made between the RHK SPM 100 and the lock-in amplifier.

If everything appears to be working, install the real sample to the STM and approach the tip to the sample again to make sure a tunnel junction can be formed on this sample. At this point, one can prepare to cool down the cryostat.

B. Cooling Down the Cryostat

First, make sure that the STM head and all other peripheral attachments are in their correct positions; and all electrical connections are continuous and do not short to ground. Compare all the measured resistances to their values from previous cool downs. Nominal values of these resistances at room temperature, liquid nitrogen temperature, and liquid helium temperature, are listed in Tables IV, V, and VI. After completing these checks, one can proceed to cool the cryostat down to liquid helium temperature. This is a straightforward process, involving the following steps:

- 1) Clean the o-ring grooves on the 4 K flange and vacuum can with methanol and assemble the vacuum can and tail to the 4 K flange with fuse wire (0.025 in in diameter) o-rings [51]. There are white indicator markings on the vacuum can, tail, and 4 K flange that must be aligned on mating pieces. Twenty-four 6-32 stainless screws with brass washers are used.
- 2) Start the leak detector and use the diffusion pump to pump down the vacuum can for an entire night. There are two pressure gauges; one is connected to the vacuum can (TC2) at the top of the cryostat and the other (PG2) is in the pumping line on the gas panel. Make sure that TC2 is less than

Table IV. Nominal Resistance Values at Room Temperature

Time: 4:50 pm	Temperature: Room	Date: 05/14/08
Sample Heater: 698.6 Ω	⁴ He Stage Heater: 534.8 Ω	³ He Stage Heater: 569.3 Ω

Bath Thermometer, 4 wires: 475.3 Ω

G-H	703.2 Ω	H-L	227.7 Ω
G-L	703.0 Ω	H-M	703.0 Ω
G-M	227.7 Ω	L-M	702.9 Ω

⁴He Spear Stage Thermometer, 4 wires: 540.1 Ω

1-2	183.5 Ω	2-3	725.7 Ω
1-3	724.3 Ω	2-4	725.3 Ω
1-4	723.9 Ω	3-4	185.3 Ω

³He Spear Stage Thermometer, 4 wires: 273.0 Ω

1-2	209.0 Ω	2-3	482.0 Ω
1-3	482.0 Ω	2-4	481.0 Ω
1-4	481.0 Ω	3-4	207.0 Ω

Calibrated C7379 Thermometer, 4 wires: 8.06 Ω

1-2	204.07 Ω	2-3	212.67 Ω
1-3	213.32 Ω	2-4	212.08 Ω
1-4	212.73 Ω	3-4	205.20 Ω

LHe Level Detector I, 4 wires: 389.7 Ω

1-2	526.0 Ω	2-3	131.5 Ω
1-3	526.0 Ω	2-4	520.5 Ω
1-4	135.8 Ω	3-4	520.5 Ω

LHe Level Detector II, 4 wires: 475.9 Ω

1-2	686.4 Ω	2-3	205.7 Ω
1-3	686.5 Ω	2-4	681.1 Ω
1-4	210.2 Ω	3-4	681.2 Ω

Table V. Nominal Resistance Values at Liquid Nitrogen Temperature

Time: 1:45 pm	Temperature: LN ₂	Date: 05/25/08
Sample Heater: 683.2 Ω	⁴ He Stage Heater: 523.3 Ω	³ He Stage Heater: 556.6 Ω

Bath Thermometer, 4 wires: 553.8 Ω

G-H	771.6 Ω	H-L	217.6 Ω
G-L	771.4 Ω	H-M	771.4 Ω
G-M	217.6 Ω	L-M	771.2 Ω

⁴He Spear Stage Thermometer, 4 wires: 632.2 Ω

1-2	178.1 Ω	2-3	812.3 Ω
1-3	811.0 Ω	2-4	811.9 Ω
1-4	810.6 Ω	3-4	179.9 Ω

³He Spear Stage Thermometer, 4 wires: 311.3 Ω

1-2	202.2 Ω	2-3	512.5 Ω
1-3	513.5 Ω	2-4	513.4 Ω
1-4	512.5 Ω	3-4	200.9 Ω

Calibrated C7379 Thermometer, 4 wires: 13.98 Ω

1-2	200.01 Ω	2-3	214.74 Ω
1-3	215.40 Ω	2-4	213.93 Ω
1-4	214.58 Ω	3-4	201.35 Ω

LHe Level Detector I, 4 wires: 346.8 Ω

1-2	479.1 Ω	2-3	127.5 Ω
1-3	479.1 Ω	2-4	473.8 Ω
1-4	131.6 Ω	3-4	473.7 Ω

LHe Level Detector II, 4 wires: 424.1 Ω

1-2	626.9 Ω	2-3	197.9 Ω
1-3	626.8 Ω	2-4	621.7 Ω
1-4	202.4 Ω	3-4	621.5 Ω

Table VI. Nominal Resistance Values at Liquid Helium Temperature

Time: 6:35 pm	Temperature: LHe	Date: 04/15/09
Sample Heater: 655.3 Ω	⁴ He Stage Heater: 501.7 Ω	³ He Stage Heater: 534.0 Ω

Bath Thermometer, 4 wires: 888.8 Ω

G-H	1096.8 Ω	H-L	207.8 Ω
G-L	1096.5 Ω	H-M	1096.7 Ω
G-M	207.7 Ω	L-M	1096.4 Ω

⁴He Spear Stage Thermometer 4 wires: 1056.7 Ω

1-2	172.8 Ω	2-3	1231.2 Ω
1-3	1230.0 Ω	2-4	1230.9 Ω
1-4	1229.6 Ω	3-4	174.9 Ω

³He Spear Stage Thermometer, 4 wires: 486.1 Ω

1-2	195.6 Ω	2-3	681.6 Ω
1-3	681.6 Ω	2-4	680.7 Ω
1-4	680.8 Ω	3-4	194.5 Ω

Calibrated C7379 Thermometer, 4 wires: 561.5 Ω

1-2	450.3 Ω	2-3	1030.3 Ω
1-3	1055.7 Ω	2-4	986.1 Ω
1-4	1011.7 Ω	3-4	490.5 Ω

LHe Level Detector I, 4 wires: 0.004 Ω

1-2	126.84 Ω	2-3	122.56 Ω
1-3	126.87 Ω	2-4	121.95 Ω
1-4	126.26 Ω	3-4	121.98 Ω

LHe Level Detector II, 4 wires: 0.001 Ω

1-2	193.00 Ω	2-3	188.55 Ω
1-3	193.14 Ω	2-4	188.15 Ω
1-4	192.75 Ω	3-4	188.29 Ω

$1.0 \times 10^{-2} \text{ Torr}$ and PG2 is less than $7.0 \times 10^{-3} \text{ Torr}$. The leak detector will remain on during the whole experiment.

- 3) Perform a room temperature leak check with the leak detector. Spray ^4He gas at various connections on the vacuum control panel, all tubes and connections of the cryostat, and fuse wire o-rings and screws of the vacuum can and tail to search for any leaks. The leak rate should be almost equal to or just slightly larger than the background leak rate that usually is $2.5 \times 10^{-8} \text{ cc/sec}$ at 1 atm . Keep the vacuum can under vacuum until Step 11.
- 4) Measure the capacitances of the level capacitor in the ^4He pot when the ^4He pot is filled with air (24.459530 pF), under vacuum (24.435663 pF), and filled with ^4He gas (24.437457 pF). Compare these capacitances with those measured in previous experiments. When the ^4He pot is filled of ^4He gas, observe the leak detector to see whether there are any leaks from the ^4He pot.
- 5) A 1.3 hp variable-speed winch mounted on the top of the cryostat is used to raise the superconducting magnet up to the middle flange between the vacuum can and the vacuum can tail. Two steel cables are connected to two eye hooks attached to the aluminum ears of the magnet adapter mounted to the top of the magnet. The magnet should be slowly and carefully raised around the vacuum can tail. The magnet adapter should be fastened to the two stainless steel magnet support rods with two 1/4-20 stainless steel screws. Then fasten the magnet adapter to the middle flange with twelve 1/4-20 stainless steel screws. At this point, the cables used to raise the magnet

can be lowered. They will be used again to raise the Dewar. Connect the magnet to the power supply through the two magnet leads which are made from OFHC copper connectors and long ribbons made from Alloy 210 Brass. Connect all the diagnostic wires for measuring voltages along the magnetic cables and for operating the persistent heat switch.

- 6) Insert a liquid nitrogen transfer tube into the cryostat and screw it into the transfer tube extension whose lower end is a gently curved black PVC tube that rests almost horizontally on the bottom of the Dewar. The upper end of the transfer tube extension is a brass, threaded bowl mounted to the 4 K flange that can mate with the liquid nitrogen transfer tube and the liquid helium transfer tube. The liquid nitrogen transfer tube is a 40 *in* long piece of thin-walled 0.375 *in* O.D. stainless steel tubing, with a hollow, threaded, nylon nut at the bottom. This nut screws into the cup of the transfer tube extension, forming an adequate seal so that liquid nitrogen (LN₂) entering the top of the cryostat will flow all the way to the bottom of the Dewar.
- 7) All the wires, the transfer tube extension, and the two ⁴He filling capillaries with two valves must be bound to the magnet surface by either dental floss or masking tape in order to make sure that they will not catch on the Dewar as it is raised.
- 8) Clean the Buna-N o-ring and the top flange of the Dewar. The two steel cables of the power winch are aligned to fit through holes in the top flange of the Dewar and attach to the lifting ears on its side. A bubble level is used to

help adjust the length of the steel cables to make the top flange horizontal. Lift up the Dewar slowly and carefully over the magnet, can, and six baffles; and then fasten it to the underside of the Room Temperature Plate with ten 5/16-18 stainless steel screws.

- 9) Use the diffusion pump of the leak detector to pump out the vacuum space of the Dewar for at least 12 hours so that the reading of the pressure gauge on the leak detector is less than 10^{-5} Torr in order to form a good thermal barrier. A special tool is used to open and close the steel ball bearing that seals the vacuum space to atmosphere.

- 10) Pump out the liquid space of the Dewar with the ^4He pump to -1000 mbar .

Fill ^4He gas into this space to approximately 1 atm pressure, so that all the parts of the cryostat inside the Dewar are surrounded by ^4He gas. Monitor the leak detector again to see whether there are any leaks into the vacuum can at room temperature. Keep the ^4He gas in the Dewar for more than 20 minutes to make sure that there are no small or slow leaks.

- 11) Fill ^4He gas into the ^4He pot ($> 1 \text{ atm}$) and pressurize the two small CuNi ^4He filling capillaries from a high pressure ^4He gas bottle to about 45 psi by opening the fast/slow pressure valves at the top of the cryostat. This is to prevent any liquid or gaseous nitrogen introduced into the Dewar in Step 13 from entering the capillaries and ^4He pot. If nitrogen does enter the filling

lines, it would eventually freeze during the helium transfer and form a irremovable obstruction.

12) Admit a small amount of Neon gas ($\sim 2\text{Torr}$) into the vacuum can as thermal exchange gas in order to increase the thermal conduction between the walls of the vacuum can and the inner parts of the cryostat. If there were no thermal exchange gas inside the vacuum can, it would take days for the cryostat to cool from radiative processes only. The boiling point of the Neon gas is around 27 K at one atmosphere, so it can at most help to cool the cryostat down to 27 K .

13) Transfer liquid nitrogen into the Dewar by directly connecting a 160l portable high pressure liquid nitrogen tank to the liquid nitrogen transfer tube using a flexible rubber hose. Because liquid nitrogen is much cheaper and has a greater latent heat than liquid helium, we use liquid nitrogen to cool the cryostat down from room temperature to its boiling point at one atmosphere, 77.4 K , for the first cooling step. To cool the cryostat further one uses liquid helium to cool down to 4.2 K , the boiling point of liquid helium at one atmosphere. It usually takes around 50 liters of LN_2 and 18 hours to cool the cryostat and magnet from room temperature to 77.4 K . Two thermometers are used to monitor the temperatures of two important parts of the cryostat during the cooling process; the C7379 thermometer is on the ^3He pot stage and the DT-670 thermometer is on the sample holder receptacle of the STM

head. C7379 shows a slightly higher temperature (20 to 30 K difference) than does DT-670 since it is at a higher position in the cryostat, but when the whole cryostat reaches 77.4 K , the two thermometers show almost the same temperatures.

- 14) As the temperature of the cryostat approaches 77.4 K , use the leak detector to pump out the vacuum can until TC2 is less than $1.0 \times 10^{-2} \text{ Torr}$ and PG2 is less than $7.0 \times 10^{-3} \text{ Torr}$, and keep it under vacuum through Step 17. Approach the tip to the “in range” position, scan the sample, and take $I \sim V$ and $\frac{dI}{dV} \sim V$ curves in order to make sure that the STM is working well at liquid nitrogen temperature.
- 15) If there are no problems with either the STM or the cryostat at liquid nitrogen temperature, then in preparation for transfer of liquid helium all of the liquid nitrogen must be removed from the Dewar. To do so, pressurize the Dewar by filling with high pressure dry gaseous nitrogen. By adjusting the nitrogen gas regulator to a suitable pressure (the pointer of the Bath Pressure Gauge should be in “C” position), the liquid nitrogen will be push out from the top of the cryostat through the liquid nitrogen transfer tube. Collect the liquid nitrogen for future use.
- 16) All of the liquid nitrogen must be completely removed from the Dewar; otherwise it could block the ^4He filling capillaries as the temperature of the cryostat is lowered in later steps. This is done by repeatedly evacuating the

Dewar with the ^4He pump and backfilling with dry nitrogen gas. During the pumping and flushing process, one should monitor the resistance of the bath thermometer which lies on the bottom of the Dewar. If any liquid nitrogen remains in the Dewar, the bath thermometer will cool upon pumping, and the resistance will increase. If the resistance does not change or increase after several cycles of pumping and flushing process, this means that the liquid nitrogen has been completely removed.

- 17) Pump out the Dewar using the ^4He pump to -1000mbar . Fill ^4He gas into the Dewar to approximately 1atm pressure and monitor the leak detector again. As the temperature decreases, any object will shrink in size. This thermal contraction could cause seals to crack and therefore it is necessary to make sure that no leaks have occurred during the cooling procedure. Again, one should keep the ^4He gas in the Dewar for more than 20 minutes to make sure that there are no small or slow leaks.
- 18) Refill Neon gas ($\sim 2\text{Torr}$) into the vacuum can as the exchange gas in order to form a thermal link between the vacuum can and the inner parts of the cryostat in later cooling steps.
- 19) Remove the liquid nitrogen transfer stick from the cryostat. There are two liquid helium transfer tubes, one is inserted into the cryostat to replace the nitrogen tube and the other is inserted into the 100l liquid helium storage Dewar. When transferring liquid helium, these two tubes should be connected and sealed together. The helium transfer tubes are different from the nitrogen

transfer tubes; as they are “mini” Dewars, constructed of two concentric stainless steel tubes with an evacuated space in between. This allows the helium liquid to transfer at 4 K through the inner tube while the outer tube remains at room temperature, otherwise a tremendous amount of liquid would boil away during a transfer. Use the diffusion pump on the leak detector to pump out the vacuum space of the helium transfer tubes for several hours before using them, making sure that the reading of the pressure gauge on the leak detector is less than 10^{-5} Torr to insure a good thermal insulation.

20) Clean helium gas from a high pressure bottle is used to pressurize the liquid helium surface in the storage Dewar to push the liquid helium out of the storage Dewar and into the Dewar through the helium transfer tubes. There is a flow meter valve that can adjust the flow of helium gas into the storage dewar to control the transfer rate. To insure an efficient transfer in which the inner parts of the vacuum can are in good thermal equilibrium with the walls of the vacuum can, one must carefully monitor the bath thermometer, the TC2 pressure gauge which shows the Neon gas pressure in the vacuum can, the C7379 and Dt-670 thermometers that measure the temperatures of the ^3He pot stage and the sample holder receptacle. During the transfer, one should carefully control the transfer rate to keep the resistance of the bath thermometer less than $\sim 710\Omega$ (i.e. below its resistance at liquid helium temperature) and the TC2 reading larger than 100 mTorr , which is the minimum pressure to maintain a relatively good thermal conduction. The

purpose of a slowly paced transfer (rather than simply gushing in liquid helium), is to take advantage of the enthalpy of the helium vapor to cool the magnet and vacuum can. If liquid helium is transferred too quickly and collects in the bottom of the Dewar while the temperature of the cryostat is relatively high, the liquid helium would boil away quickly and would be wasted. It takes about six hours to cool the cryostat down to 27 K with this cooling method. As the temperature of the inner cryostat reaches the boiling point of Neon, no more cooling will take place as all of the Neon gas condenses onto the walls of the vacuum can. At this point, one may begin filling the Dewar with liquid helium at a faster transfer rate. Typically, about 50 l of liquid helium is required to fill the Dewar up to the first baffle which is nine inches above the 4 K flange. During the transfer, the ^4He pot should be pressurized with helium gas ($>1\text{ atm}$). Once the liquid helium bath completely covers the upper pumping line which leads into the ^4He pot, any helium gas below the first baffle will condense into liquid and flow downward into the ^4He pot, thereby quickly cooling the ^4He pot to 4.2 K . Two calibrated level detectors (a piece of superconducting wire vertically spanning the length of the vacuum can and magnet) can be used to determine how much liquid helium is in the Dewar at any time. It takes about a half day to cool the entire cryostat down to 4.2 K .

- 21) After the vacuum can is surrounded by liquid helium, one should pump out the vacuum can and do another leak detection to see if any leaks or cracks

have occurred during this cooling procedure. At this point, one has completed four leak detections in total.

22) Once the entire cryostat is at liquid helium temperature, the ^4He Pot is sufficiently cold to sustain liquid inside. One can open the fast/slow vacuum valves to allow the liquid helium to be transferred from the bath to the ^4He pot, and start the ^4He pump. Immediately, both the pressure and temperature should drop as the pump removes vapor from the surface of the liquid within the ^4He pot. With the slow vacuum valve open, the ^4He pot will be constantly replenished from the bath. By continuously pumping the ^4He pot, our cryostat can reach a temperature of 1.2 K within a few hours.

The surface level of liquid helium in the bath will continuously drop over time, affecting the cooling power of the cryostat, as well as the temperature of STM head. The boil off rate for the liquid helium is shown in Figure 13. As previously mentioned, there are two liquid helium level detectors installed in the cryostat. The level detector I is used to measure the liquid level from the 4 K flange to almost the bottom of the vacuum can tail and level detector II runs from the first baffle down to the bottom end of the superconducting magnet. According to Figure 13, if liquid helium is filled up to the first baffle, it will run out in about two days. Therefore one must refill liquid helium into the bath every two days in order to keep the cryostat and the STM head cold enough for the experiments.

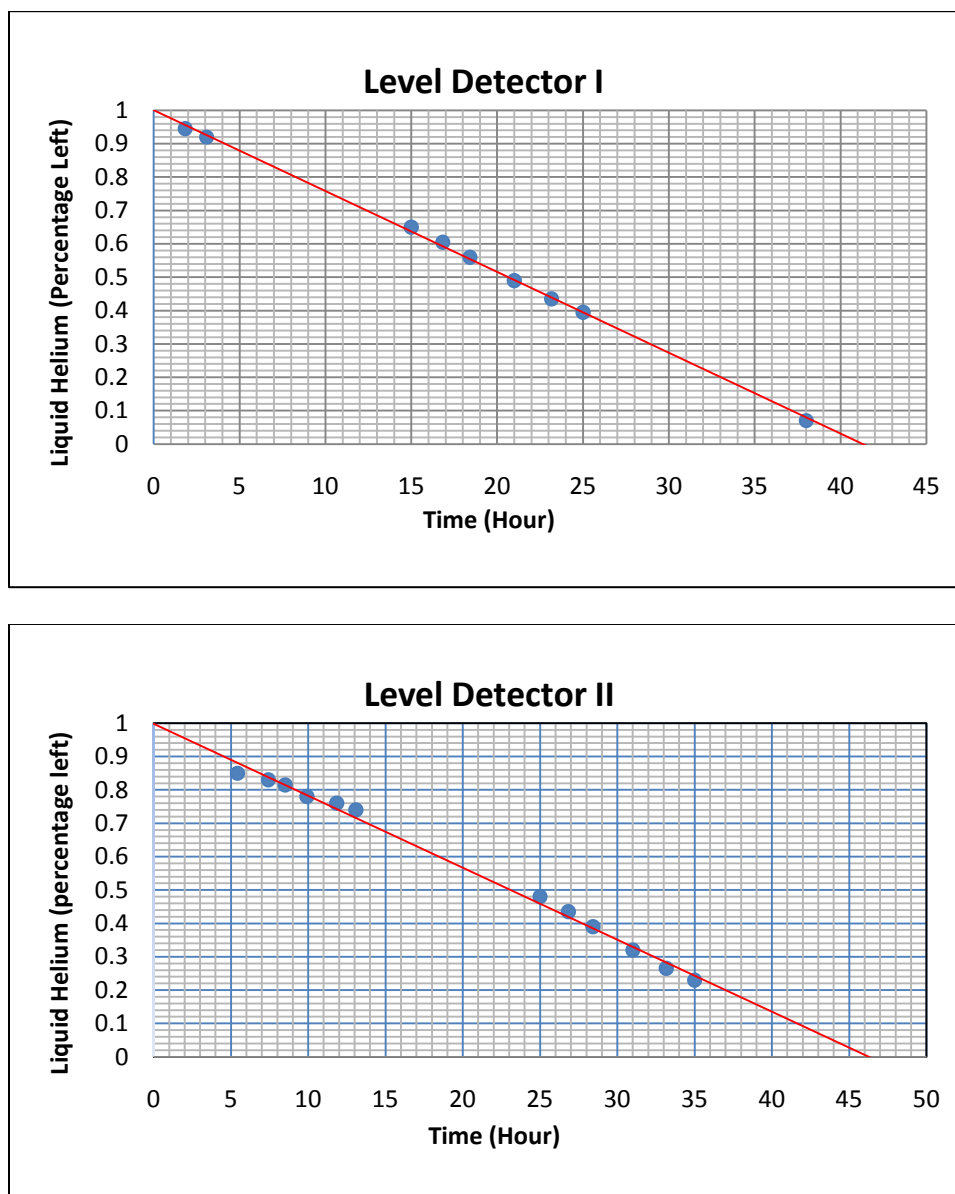


Figure 13. Graphs of the liquid helium boil off rate. The liquid helium level drops at a constant rate over time.

C. Data Acquisition

The topography of the sample surface, the current I and differential conductance dI/dV of the tunnel junction are all measured and analyzed by the data acquisition system shown in Figure 14. This system consists of the cryostat and the STM head, the current preamplifier set, the lock-in amplifier, the RHK SPM 100 control box, the ratio transformer, and the remote control computer.

The current preamplifier set includes two stages; the first stage is the IVP-200 current preamplifier which outputs $100mV$ per $1nA$ of input; the second stage is the multi-gain preamplifier which amplifies the output of the first stage by a gain of 1, 10, or 100. Our STM has a wide working range from $10pA$ to $10nA$.

The RHK SPM 100 is the control electronics, that provides the DC bias voltage to the tunnel junction, controls the piezoceramic tube scanner in the x, y and z directions, and analyzes the output signal from the preamplifier set and the lock-in amplifier. A topography image is generated by recording the control voltage for the z- motion of the scanning tube as the tip is scanned across the sample surface.

The SPM 100 controller can also provide a ramping bias voltage for measurements of the current and differential conductance of the tunnel junction. No additional equipment is needed to determine the current versus bias voltage curves as both signals (current and bias voltage) are automatically recorded by the SPM 100. To measure the differential conductance, one can use a technique in which the bias voltage is modulated with a small ac component. A $2000Hz$, $1.0V$ amplitude sine wave generated by the lock-in amplifier is reduced to a small AC modulation voltage

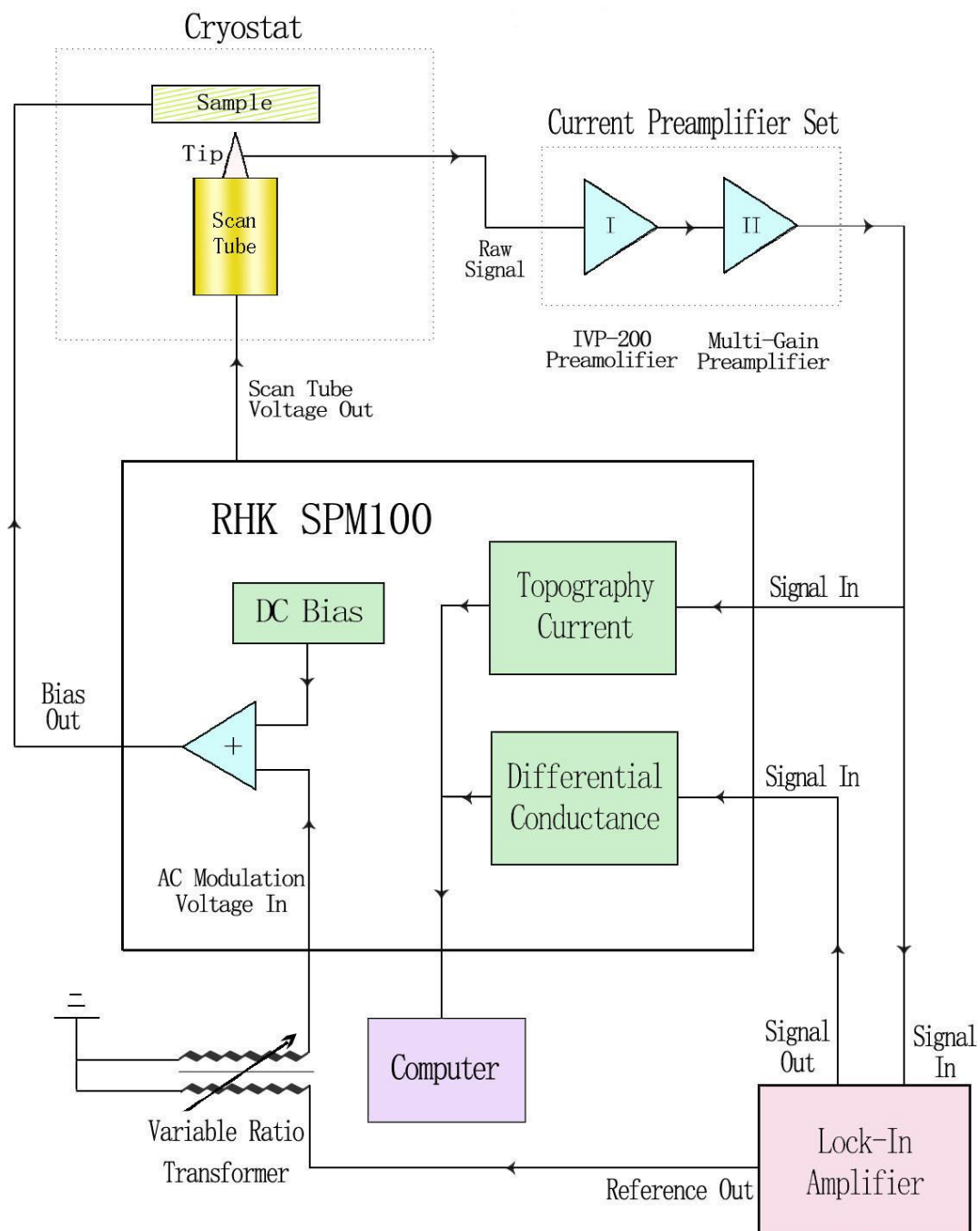


Figure 14. Schematic of the data acquisition circuit.

(0.2 to 1mV) by a variable ratio transformer and then added to the ramping bias voltage. To understand how the differential conductance dI / dV is detected, consider a small modulation voltage applied to the bias voltage. The bias voltage can be written as $V = V_{DC} + \Delta V \cos(\omega t)$, where ΔV and ω are the amplitude and the frequency of the AC modulation voltage. If ΔV is much smaller than the DC voltage, one can expand the current in a Taylor's series

$$I = I(V_{DC}) + \Delta V \cos(\omega t) \left. \frac{dI}{dV} \right|_{V=V_{DC}} + O(\Delta V^2) \quad (3.1)$$

The measured current therefore has an AC component at frequency ω that can be detected by the lock-in amplifier.

The differential conductance dI / dV is calculated from the output voltage of the lock-in amplifier,

$$\frac{dI}{dV} = \frac{(Preamplifier \text{ sensitivity}) * (Lock-in \text{ sensitivity}) * V_{lock-in}}{10 * (\Delta V / \sqrt{2})} \quad (3.2)$$

where $V_{lock-in}$ is the DC output of the lock-in, *Preamplifier sensitivity* is the combined gain of the current preamplifier set, *Lock-in Sensitivity* is the DC gain setting on the lock-in, the fact of 10 is the full scale output of the Lock-in amplifier.

CHAPTER IV

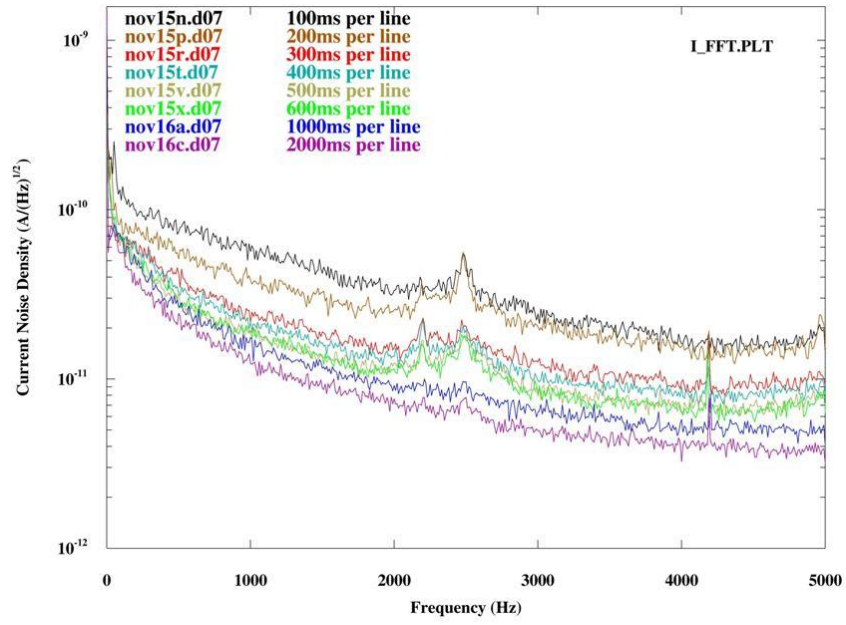
RESULTS AND DISCUSSION

A. Tunneling Noise and Analysis

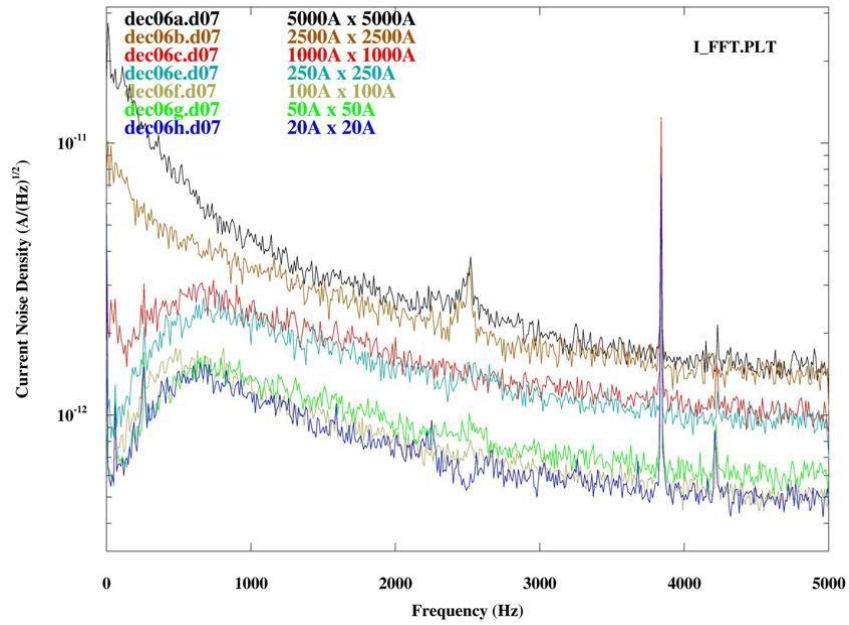
STM measurements of the surface topography or local electronic density of states put high demands on the mechanical stability of the STM and the entire cryostat. In addition to the methods used to stabilize the STM system described in Chapter II, it is also important to consider some of the operational parameters associated with the actual data acquisition.

One such parameter is the speed at which the tip is scanned across a sample during a measurement of the topography of the sample surface. The image obtained by the STM is typically 256 x 256 pixels. The scanning speed is defined by the amount of time that the STM tip takes to scan a single line across the sample. In Figure 15, the current noise density (A/\sqrt{Hz}) is plotted as a function of the frequency. All the data was taken with a bias voltage of 0.02V and a current setpoint of 1.0nA.

In Figure 15a, the scanning area is fixed at 2500Å x 2500Å and the scanning speed is changed. Clearly the current noise increases with an increase in the scanning speed. Figure 15b shows a similar dependence when the scanning speed is fixed at 300ms/line but the scan area is changed. As the scanning area is increased corresponding to an increase in the scanning speed, the current noise level also increases.



(a)



(b)

Figure 15. Current noise density measured at different scanning speed or different scanning area. (a) Fixed scanning area with different scanning speeds. (b) Fixed scanning speed with different scanning areas.

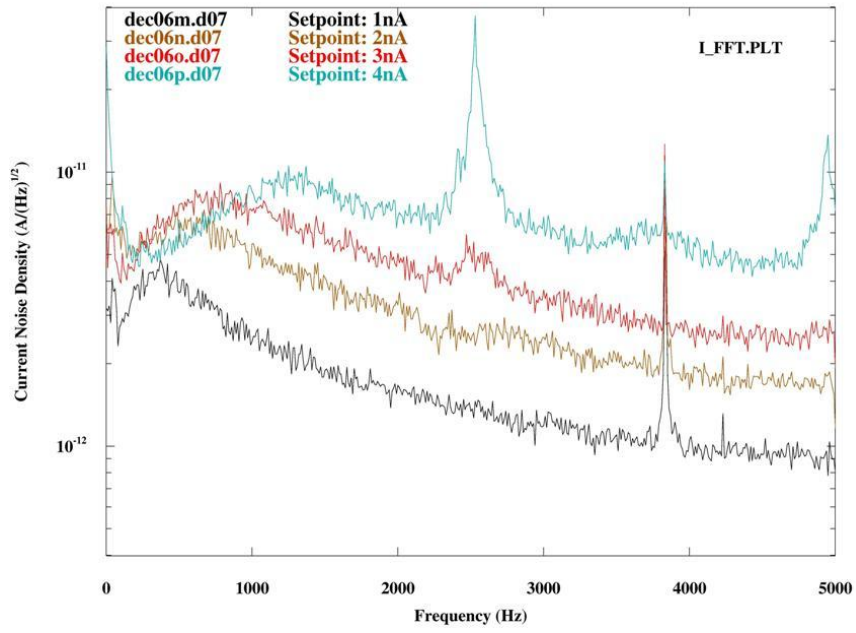
In practice, the proper scanning speed setting is determined by the size of the scan area and the roughness of the sample surface. The smaller the scanning area and the smoother the surface, the faster the scanning speed can be set.

According to the tunneling current equation, $I = CV_b \exp(-D\sqrt{\phi}d)$; the tip-sample separation d is determined by the current setpoint and the bias voltage. If the current setpoint and bias voltage remain constant and the ambient noise causes a small change in the separation, Δd , there will be a corresponding noise in the tunneling current. This current noise ΔI is given by

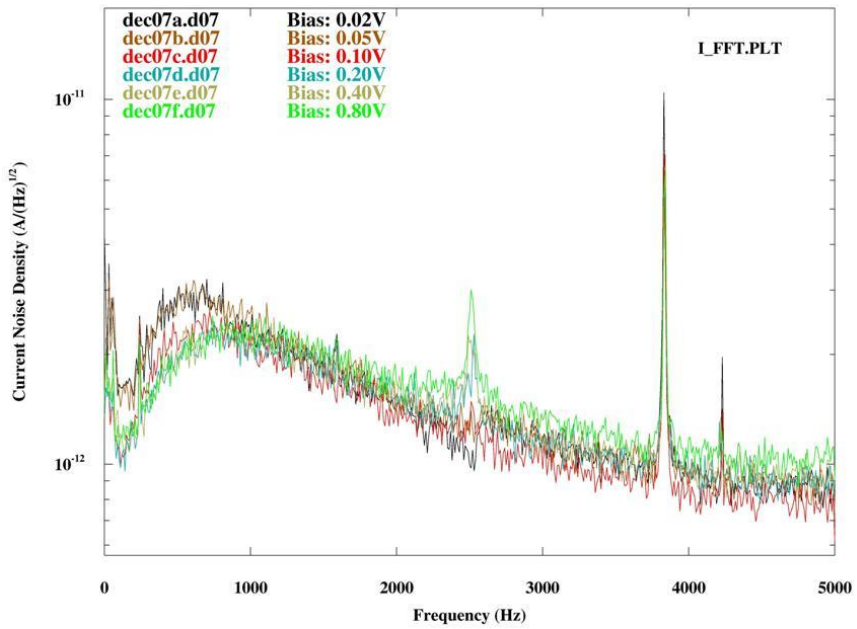
$$\begin{aligned}\Delta I &= I(d_0 + \Delta d) - I(d_0) = I(d_0) \left(\exp(-D\sqrt{\phi}\Delta d) - 1 \right) \\ &= -I(d_0) \left(D\sqrt{\phi}\Delta d \right) + O(\Delta d^2)\end{aligned}\tag{4.1}$$

Therefore, given the same amount of vibration noise Δd , the current noise should scale with the value of the current setpoint.

One can verify this equation by measuring the current noise while keeping either the tip-sample separation or the current setpoint fixed as the STM scans a sample surface. These results are shown in Figure 16. All of the data was taken at a scanning speed of $300\text{ms}/\text{line}$ with a scanning area of $1000\text{ \AA} \times 1000\text{ \AA}$. In Figure 16a, the tip-sample separation is kept constant by keeping the ratio of the bias voltage and the current setpoint constant. In agreement with the above equation, the current noise increases as the current setpoint is increased.



(a)



(b)

Figure 16. Current noise density measured at different current setpoints or different bias voltages. (a) Fixed tip-sample separation with different bias voltage-current setpoint pairs. (b) Fixed current setpoint with different bias voltages.

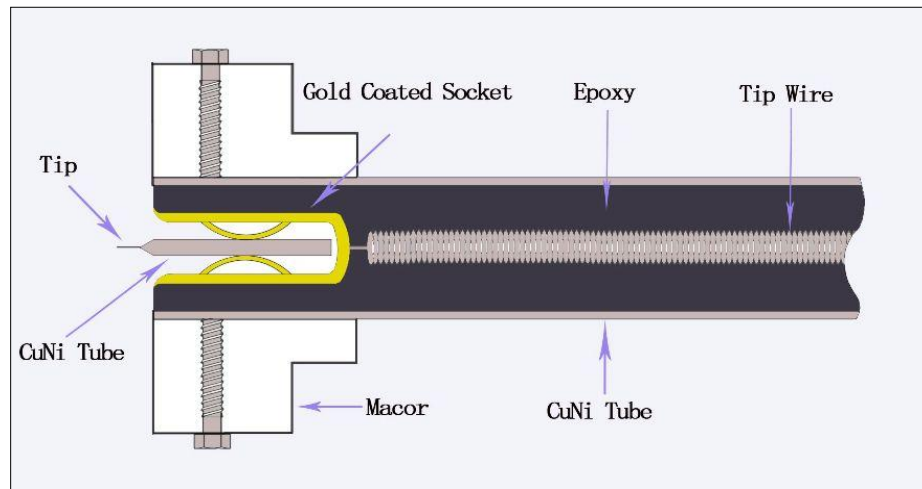
In Figure 16b, the bias voltage is increased from $0.02V$ to $0.80V$ while keeping the current setpoint constant at $1nA$. Equivalently, this corresponds to increasing the tip-sample separation while keeping the current setpoint constant. As expected, the current noise remains at approximately the same level. We can conclude then that the current noise primarily comes from the small vibrations Δd in the system and depends only on the current setpoint and it is independent of the tip-sample separation and the bias voltage. As we showed previously, the main source of this vibration noise comes from the motion of the tip as it scans a surface. Therefore, the optimum setting for current setpoint will depend upon the size of the scan area and the roughness of the sample surface. The smaller the scanning area and the smoother the surface, the larger the current setpoint can be set.

Because electronic noise is also a major source of noise in tunnel junctions, one should shield the STM head as well as possible from external electronic noise. In particular, it is very important that the tip wire be completely shielded. Unfortunately, the current noise from the preamplifier increases with increasing capacitance between the tip and ground. The overall noise floor of the IVP-200 preamplifier is partially a function of the capacitance of the tip wire connected to the input BNC connector and the setting of the filter selector in the second stage multi-gain preamplifier. A better shielded tip holder, a lower tip wire capacitance, and the proper filter setting would lower the

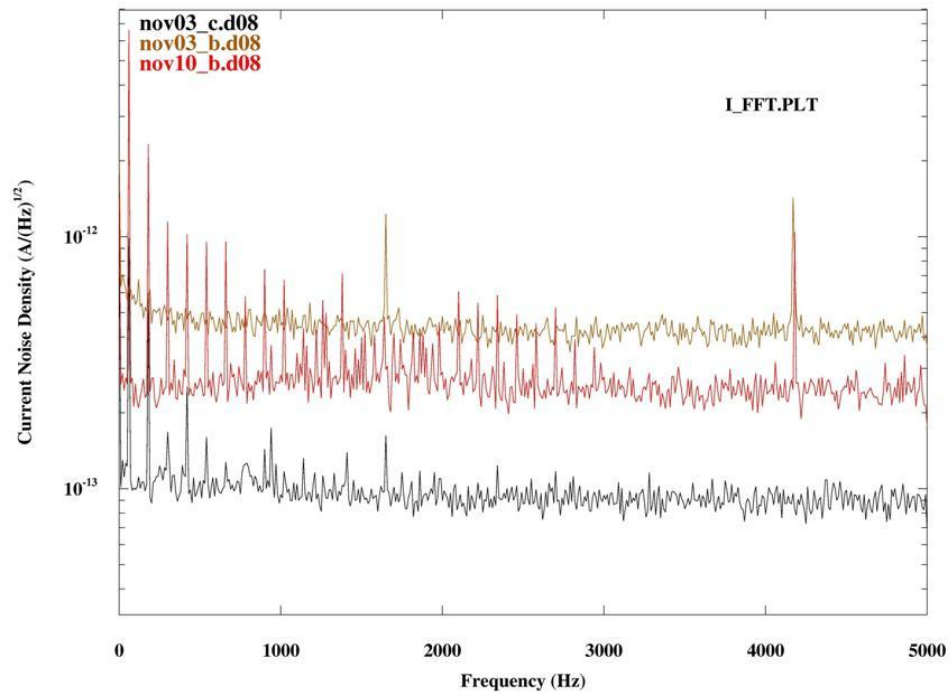
tunnel current noise level.

Figure 17a shows the structure of the new tip holder that we built for the STM. The low capacitance Cooner coaxial cable (described in Chapter II) is connected to the gold plated spring socket (Digi-Key A24850-ND, 0.050in OD, 0.030in ID, 0.260in Length), that holds the tip. A CuNi tube (0.095in OD, 0.080in ID, 1.100in Length) covers the entire socket and part of the tip wire. To electrically isolate the tube from the socket and fix the connection to the coaxial cable, a UHV compatible non-electrically conducting epoxy H74F [48] is injected between the socket and inner surface of the tube. The position of the CuNi tube is fixed by two stainless steel screws in a Macor piece that is glued on the top of the scanning tube. When the tip is inserted into the tip holder, only 2 ~ 3mm of it is outside the socket and not shielded.

There are several advantages of this tip holder; the long tube makes the tip cable more rigid thereby reducing the noise caused by vibrations, the CuNi tube shields the tip, the socket, and the tip cable very well from the scan tube wires just surround it, the measured preamplifier noise is much smaller than that measured with the old tip holder, and it is easy to change the tube and the tip cable if there is a problem. Figure 17b shows the large reduction in the current noise level associated with this new tip holder and smaller capacitance Cooner coaxial cable. Both sets of data were taken with the tip within the tunneling range but with a fixed position. For comparison, the figure also



(a)



(b)

Figure 17. (a) The structure of the tip holder. (b) Current noise levels. The black curve is the background noise, the brown curve is the noise with the previous tip holder and tip cable, the red curve is the noise with the new tip holder and tip cable.

shows the background current noise level when the IVP-200 preamplifier is open ended and therefore has no additional input capacitance. The value of the background noise is consistent with the noise level data provided with the IVP-200 manual.

B. Calibration of the STM

In order for the STM to obtain the topography of the sample surface, it requires that the x, y and z motion of the scanning tube be correctly calibrated. The scanning tube is made from PZT-4 piezoceramic material [44] with one gold electrode on its inner surface and four 90° quadrants electrodes on its outer surface. It is 0.4in in length, 0.25in in OD, and 0.02in in wall thickness. The theoretical piezoelectric conversion factors for bending in the x and y directions and for stretching in z direction are determined by the following formulas [52];

$$\frac{\Delta z}{\Delta V} = \frac{d_{31}L}{t}, \quad \frac{\Delta x \text{ or } \Delta y}{\Delta V} = \frac{0.9d_{31}L^2}{d_m t} \quad (4.2)$$

where L is the length of the tube, t is the wall thickness of the tube, d_m is the average diameter of the tube $(OD + ID)/2$, and d_{31} is a temperature dependent piezoelectric coefficient of the material. Taking the room temperature value of d_{31} to be 1.27 Å/V , the calculated value for the z direction becomes

$$\frac{\Delta z}{\Delta V} = 25 \text{ Å/V} \quad (4.3)$$

Taking into account that the total distance from the tip to the bottom end of the scanning tube is approximately 0.75in, the room temperature calculated value for the x or y

directions becomes

$$\frac{\Delta x \text{ or } \Delta y}{\Delta V} = 75 \text{ \AA/V} \quad (4.4)$$

However because the theoretical coefficients can have an uncertainty of 20%, the above calculated values are not sufficiently precise for topography information. To further calibrate the STM scanning tube, we used a commercial nano-grid calibration grating and a thin gold film.

The nano-grid calibration grating (Nanosurf BT00599) is made from a $3mm \times 3mm$ polycarbonate material that has been embossed with a $160nm$ cross pattern of a periodic ball array and then coated with a thin gold film. After measuring the periodicity of the grating, one can adjust the $\Delta x/\Delta V$ and $\Delta y/\Delta V$ settings in the SPM 100 control software, SPM 32, so that this measurement corresponds to the correct $160nm$ spacing. Figure 18a and 18b show the topography of the nano-grid calibration grating at room temperature in air with a $10mV$ bias voltage and a $1.0nA$ current setpoint; Figure 18c shows the calibration process using the software XPMPro. As shown in the figure, the average spacing is determined from a measurement over four periodic lengths. Setting $\Delta x/\Delta V = \Delta y/\Delta V = 90 \text{ \AA/V}$ in the SPM 32, the average size of one ball is measured of $157.5nm$ which is very close to the standard size of $160nm$. In this way, the bending factors of the STM scanning tube were determined at different temperatures. The nominal values are 90 \AA/V at room temperature; 54 \AA/V at liquid

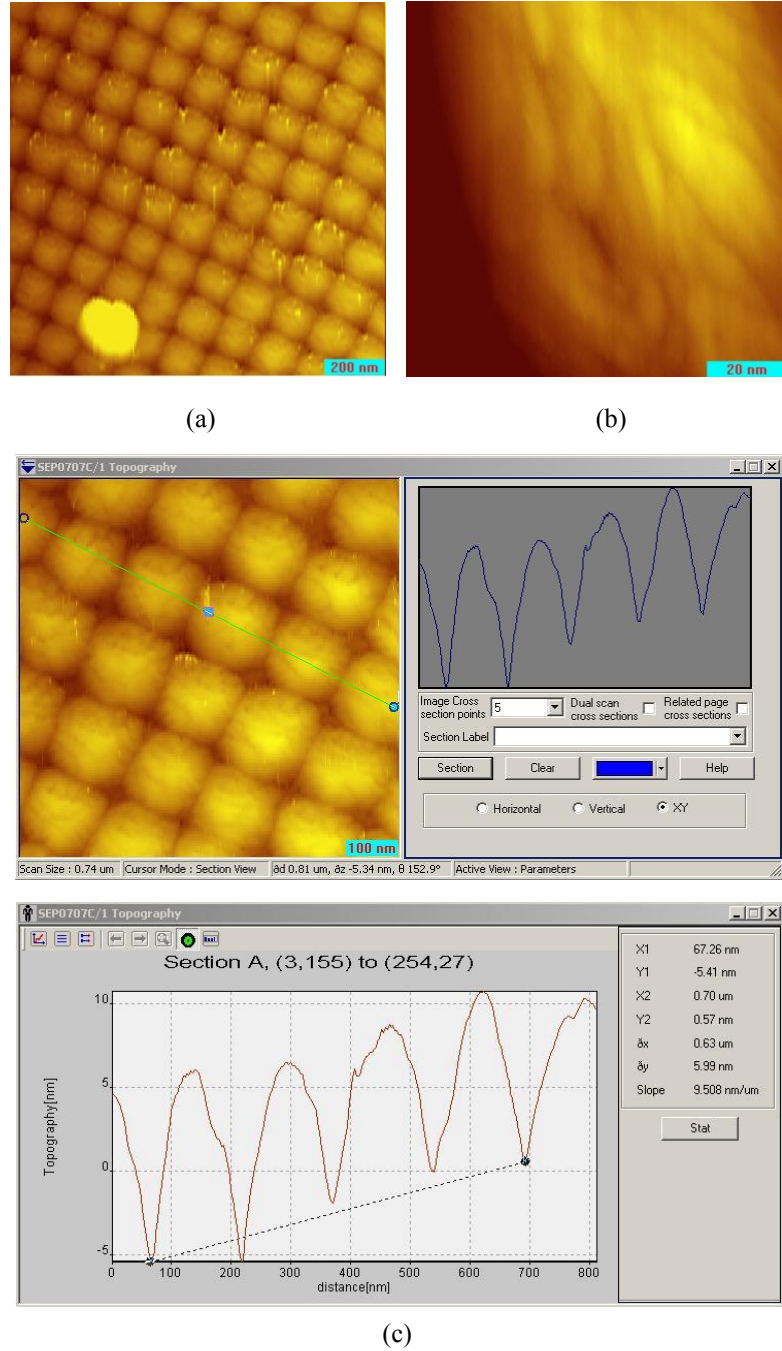


Figure 18. Room temperature calibration of the motion in the x and y directions. (a) Topography of the standard calibration surface. (b) Detailed view of one standard "ball". (c) Calibration measurements for the STM scanning tube in the x and y directions. Setting the x and y coordinate parameters in the SPM 32 to be $\Delta x/\Delta V = \Delta y/\Delta V = 90 \text{ \AA/V}$, the average size of one ball is 157.5nm which is very close to the expected size of 160nm .

nitrogen temperature, and 32 \AA/V at liquid helium temperature.

To calibrate the STM scanning tube in the z direction, one can use a thin gold film oriented in the (111) direction. The thin gold film is epitaxially grown on a cleaved mica substrate and is about 150 nm in thickness. Au (111) typically exhibits extensive terraces separated by broad steps of monolayer height. Hallmark et al [53] and Claude et al [54] observed the atomic corrugation on Au (111) with both STM and AFM and measured the height of the atomic steps, to be approximately 2.5 \AA . Figure 19a and 19b show the multi-layers on our Au (111) substrate at room temperature in vacuum with a bias voltage of 10 mV and a current setpoint of 1.0 nA . In Figure 19c, we found an atomic step between an island (90 \AA in diameter) and one layer. Setting $\Delta z/\Delta V = 24 \text{ \AA/V}$ in the SPM 32, the height of this step becomes 2.53 \AA which is very close to the known value of 2.5 \AA . With this method, the stretching factor of the STM scanning tube can be determined at different temperatures, 24 \AA/V at room temperature; 15 \AA/V at liquid nitrogen temperature, and 10 \AA/V at liquid helium temperature.

C. Demonstration of Atomic Resolution

In addition to the Au (111) substrate, we also examined flakes of natural graphite at room and liquid nitrogen temperatures. A clean atomically flat graphite surface can easily be prepared and therefore can be used to check the ability of the STM to obtain images with atomic resolution. Figure 20a shows the structure of the graphite lattice. The

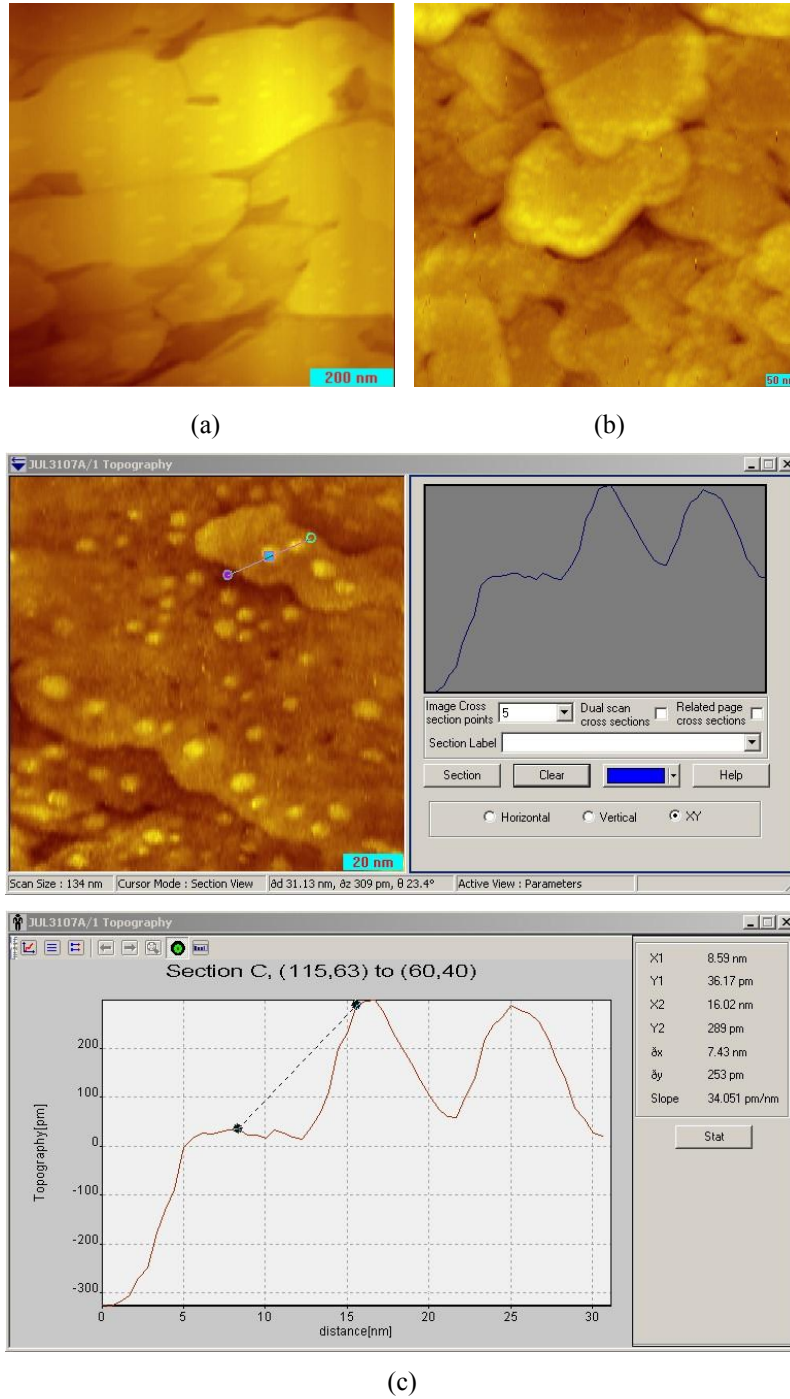


Figure 19. Thin Au (111) film on mica at room temperature. (a) Multi-layers of the Au (111) surface. (b) Detailed view of some of the layers. (c) After setting the z coordinate, parameter in the SPM 32 to be $\Delta z/\Delta V = 24 \text{ \AA/V}$, the height of one atomic step is 2.53 \AA which is very close to the published value of 2.5 \AA .

graphite surface has two types of carbon atoms, α and β , in the basis of the hexagonal surface unit cell with a next-neighbor α - β distance of 142pm and the two closest α - α and β - β distances of 246pm (Figure 20a left) [59]. The layers are stacked such that three of the six atoms within a hexagon have a direct neighbor in the layer underneath at a distance of 334pm (Figure 20a right).

To prepare a clean surface, the graphite is first mounted on the sample plate and then cleaved with adhesive tape in air. The sample plate was then immediately inserted into the STM head, the vacuum can was closed and pumped out. With this procedure, we could obtain very clear graphite surface images with our STM. Figure 20b shows the graphite surface with only the β atoms forming a triangular lattice at liquid nitrogen temperature at a bias voltage of 0.2V and a current setpoint of 1.0nA . Measuring the distance over five β atoms to be 1.2nm , one obtains the average β - β distance to be 240pm which is very close to the well known value shown in Figure 20a. This shows that our STM can achieve atomic resolution and was correctly calibrated.

Although the proverbial ease of imaging graphite by STM with atomic resolution is well documented, many previous investigations have shown that only the β atoms triangular surface structures are imaged by their STMs [55-58] whereas the α atoms remain hidden. Many people have made extensive efforts to see these hidden α atoms. Stefan *et al.* [59, 60] observed all surface atoms in graphite at 4.89K by using a low

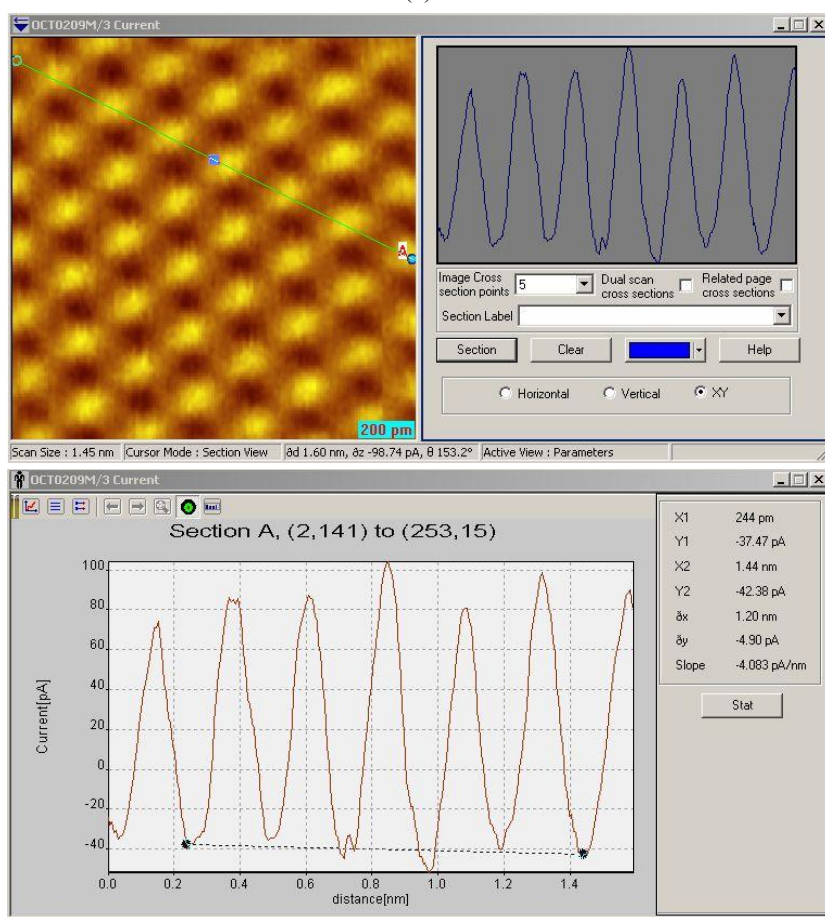
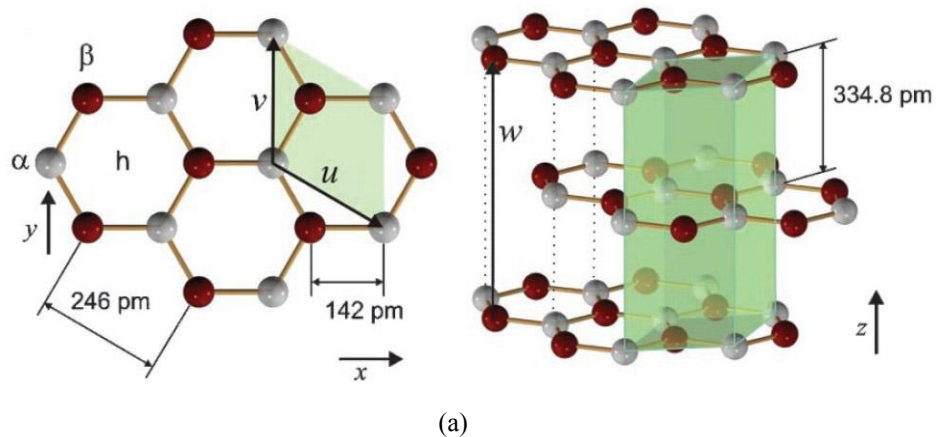


Figure 20. (a) Crystal structure of graphite. The unit cell is shaded in green. (Stefen et al., 2003). (b) Measuring the average distance between two β atoms.

temperature atomic force microscopy, but also stated that their STM could not see the α atoms at that low temperature. Many studies have been conducted in the past 20 years in order to explain this fact, but there is still no consistent explanation despite a large amount of experimental data collected. There are several theories to explain this fact; but to date there is no consensus.

D. Tománek [58] revealed a strong asymmetry of the local density of states (LDOS) at the Fermi level between α and β atoms that is determined by the interlayer interaction and the nonequivalent structure of these two types of atoms. He reported that the LDOS near the Fermi level of the β atoms was higher than that of the α atoms and therefore β atoms were more easily to be detected by an STM. Constantinos D. Zeinalipour-Yazdi and David P. Pullman [61] found that the LDOS for α and β atoms in graphite unit cell are more equivalent at higher bias voltages and they reported that only the β atoms should be detected at a bias voltage of 0.1V but both α and β atoms should be seen at a higher bias voltage of 0.7V .

The other explanation for the asymmetry is that the α and β atoms differ in their response to an external force due to different interlayer interactions [62]. In particular, the local hardness of the surface monolayer is larger for the β atoms than that of the α atoms. When the STM tip is scanning across the graphite surface, it can cause a deformation of the layer and thereby local changes in the tunneling characteristics.

Because β atoms are more difficult to deform due to their larger stiffness, they are more easily detected by the STM. Therefore the appearance of both α and β atoms hexagonal structure requires the minimal surface deformation. Atamny *et al.* [63] observed the entire hexagonal structure by a fairly large tip-sample distance that minimized the surface deformation.

These two explanations of the asymmetry are based on the interlayer interaction and therefore a single layer of graphite should not have this asymmetry problem and the entire hexagonal structure should be observed. However, Land *et al.* [64] reported that only three of the six atoms in an STM image of a single graphene layer on a Pt (111) surface. Another explanation [65] stated that the asymmetry of the carbon atoms comes from the formation of charge density waves and therefore the asymmetry should depend on the polarity of the bias voltage. However this fact contradicts many experimental data including ours.

Cisternas *et al.* [66] stated that the appearance of the full hexagonal structure of graphite should depend on narrow ranges of the tip sample distance and bias voltages. Furthermore, the tip size effect and the double atom tip explanations would not be relevant in explaining the β atoms triangle structure. He reported that the entire α and β atoms structures are only revealed at bias voltage over 0.2V and tip sample distance shorter than 2.0 Å; smaller voltages and/or larger distances would only show the β

atoms triangular structures. However, our experimental data show that the full hexagonal structure can be observed with bias voltage smaller than $0.2V$ or at a tip sample distance larger than 2.0 \AA . Overall, we believe that the graphite surface still requires additional theoretical work as well as experimental evidence to resolve this issue and that a consistent explanation of why only the β atoms are sometimes observed and sometimes all the six carbon atoms are detected is still not available.

With our STM, we can observe the hidden α atoms and obtained very clear images for the complete hexagonal surface lattice on graphite surface at liquid nitrogen temperature with a bias voltage of $0.2V$. As was reported by Yongfeng Wang et al. [67], we can also image only the β atoms triangular structure with the same tip and same bias voltage. This indicates that the bias voltage or the double-tip effect is not the reason for the α atoms to be often hidden in STM images. Figure 21 shows the 2D and 3D STM images of graphite recorded in a constant height mode at liquid nitrogen temperature with a bias voltage of $0.2V$ and a current setpoint of 1 nA . Figure 21a reveals only the β atoms triangle lattice which is similar to many previous works. Both α (white) and β (red) atoms within a hexagonal unit cell are clearly visible in Figure 21b. The hexagonal carbon rings are visible and the complete surface lattice is imaged.

We have achieved atomic resolution and found the hidden surface atoms in the unit cell of graphite and have shown the capability of our STM to gather information on

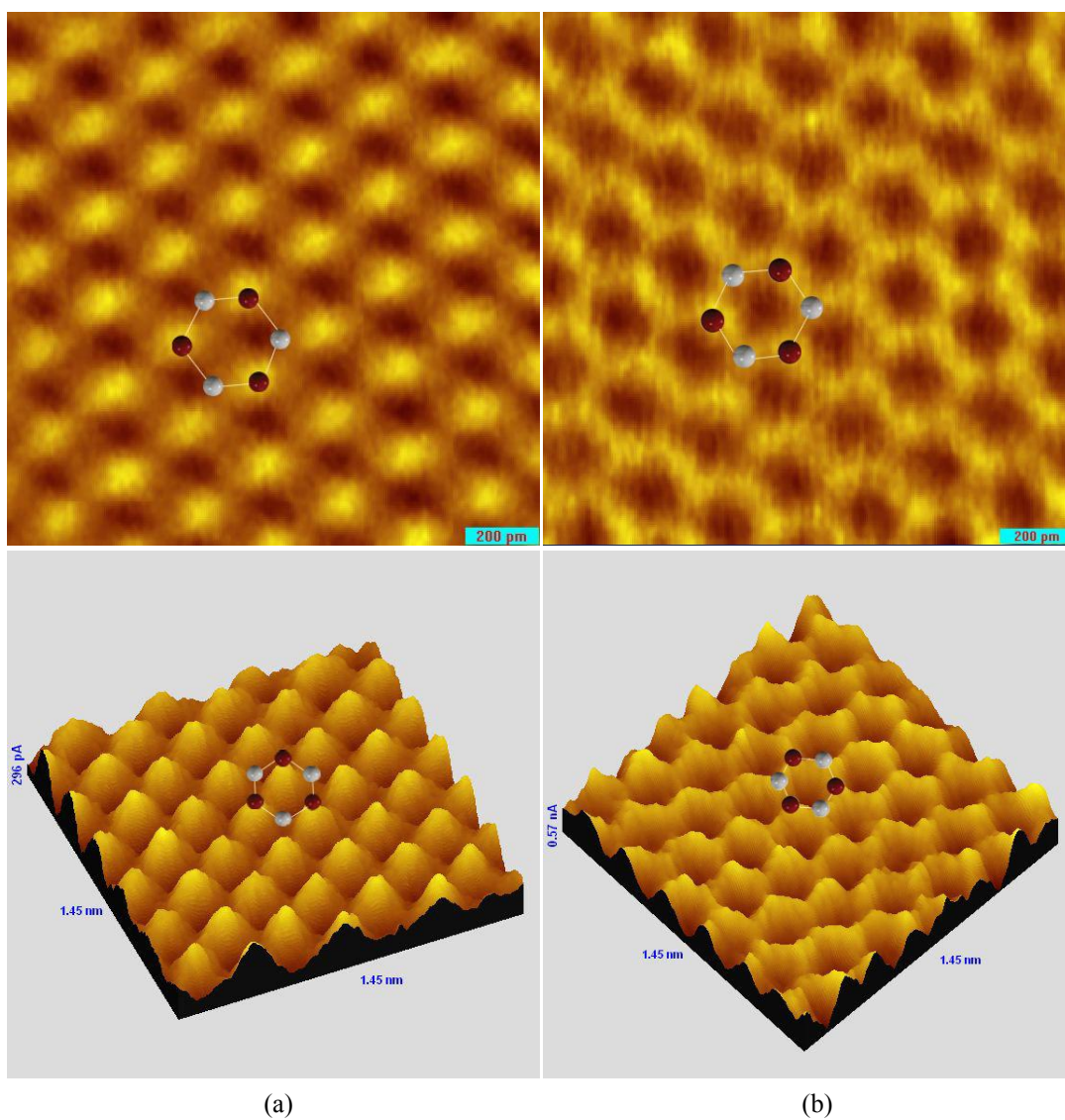


Figure 21. STM images of graphite in constant height mode with the same tip and the same bias voltage of $0.2V$. (a) The hexagonal surface unit cell has two types of carbon atoms, α (white) and β (red), in its basis but here only the β atoms are observed to form a triangular lattice. (b) Both atoms are observed and the hexagonal carbon rings are clearly visible.

surfaces that are partially accessible by some previous STMs [48-54], emphasizing an additional facet of studying soft matter on the atomic scale. The successful imaging of the complete surface lattice of graphite is encouraging regarding the possibility of imaging other materials with atomic resolution by our STM.

D. Superconductivity Studies

Utilizing our low temperature STM, we measured the current-voltage and differential conductance-voltage characteristics of the superconductor $\text{Pb}_{82}\text{Bi}_{18}$ at different temperatures: 2.09, 3.23, 4.17, 5.21, 6.23, 7.24, 8.31, and 9.04 K. PbBi is a well known superconductor with strong electron-phonon coupling and it was widely used to evaluate tunnel junctions with respect to stability and the ability to determine the electronic characteristics of the superconductor. The superconducting energy gap and transition temperature of PbBi have been measured by many groups [68-70]. The zero temperature energy gap is $2\Delta(0) = 5.4kT_c$ [68], where the superconducting transition temperature, T_c , is approximately 7.8K .

We obtained many topography images of the PbBi surface at liquid helium temperature and below. Figure 22a shows the surface images of PbBi film at 4.17K with a bias voltage of 40mV and a current setpoint of 1.0nA . The familiar superconducting energy gap feature [71] is clearly displayed in the current versus voltage plot in Figure 22b taken at 2.09K .

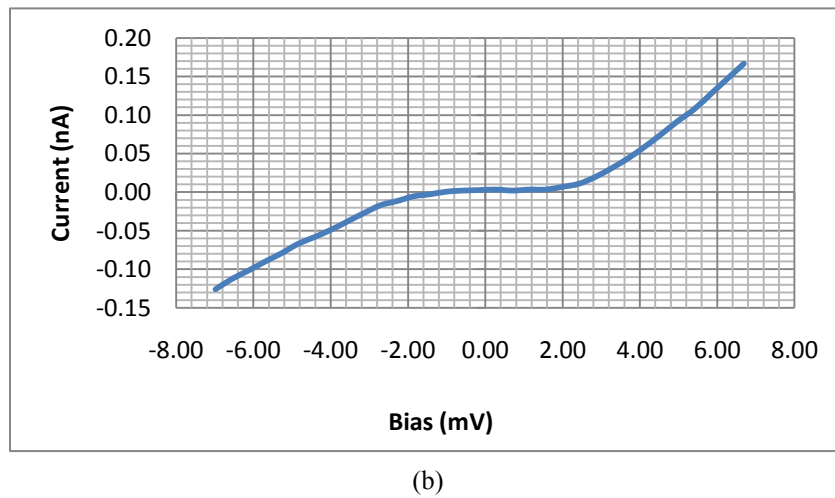
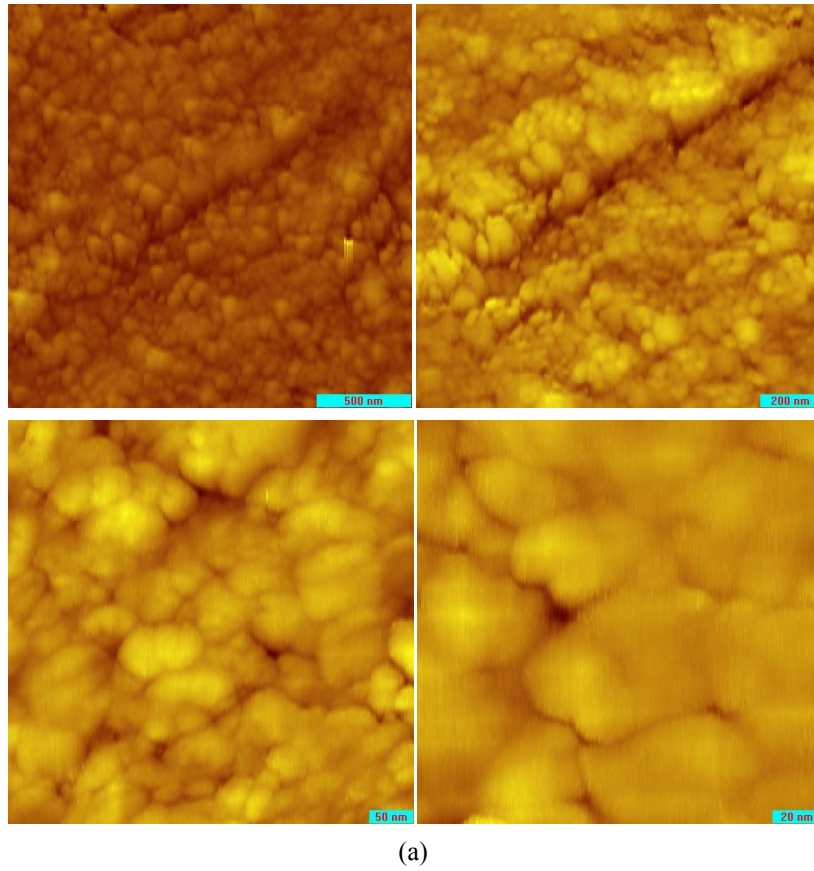
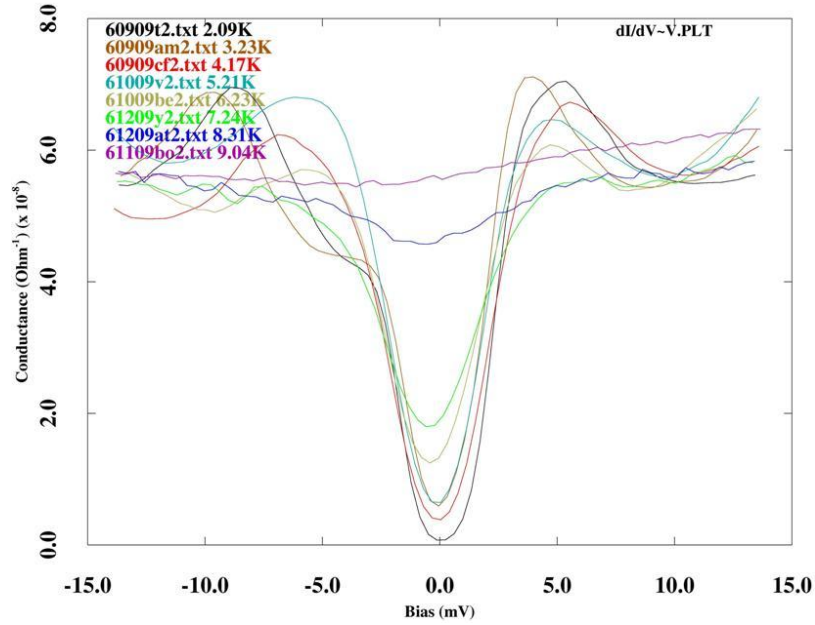
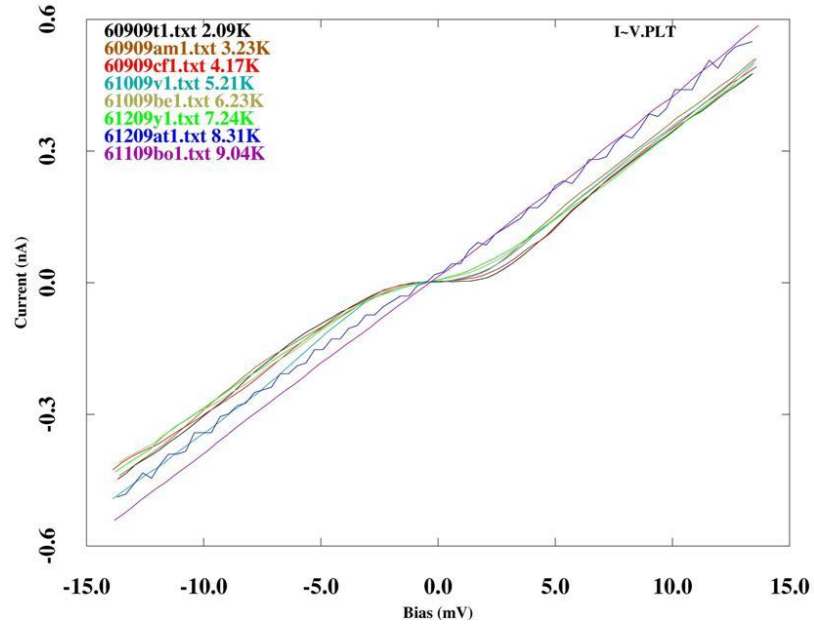


Figure 22. Topography and superconducting energy gap of a PbBi film. (a) Constant current mode topography images with different resolutions at 4.17 K . (b) Current-voltage characteristics at 2.09 K , the superconducting energy gap can be directly observed from the graph.

In Figure 23, one can easily see the differential conductance features of the energy gap and how they depend on temperature. As the temperature is increased, the width of the energy gap decreases and then reduces to zero as the temperature approaches $7.8K$. The depressed value of the zero bias differential conductances becomes smaller as the temperature increases and dI/dV versus V curves become flat when temperature is above $7.8K$.

When we attempted to fit the differential conductance curves using the BCS theory, we found that the width of the suppressed differential conductance due to the energy gaps were far too large given the published values of the energy gap. The horizontal scale appears to have been expanded by approximately a factor of four. This may have been caused by an incorrect value of the conversion factor for the D/A output that is used to sweep the bias voltage in the SPM 32 control software. Unfortunately, we do not have sufficient information to determine what correction factor should be used to rescale the data to the correct bias voltages.

However, because the value of the zero bias differential conductance is unaffected by this rescaling, it is still possible to estimate the energy gap by using the temperature dependence of the zero bias differential conductance. Evaluating the differential conductance equation numerically at zero bias and fitting our zero bias values, one can obtain the temperature dependent energy gap. Although the energy gaps



(b)

Figure 23. Measurements of the current and conductance of a PbBi film at different temperatures. The superconducting phenomena clearly disappear when the temperature is over 7.8K . (a) Current versus voltage curves. The superconducting energy gap decreases as the temperature is increases. (b) Differential conductance versus voltage curves. The depth of the depressed conductance decreases as the temperature increases.

determine in this manner have large uncertainties ($\pm 0.1K$), they agree reasonably well with the published value of the zero temperature energy gap and the BCS temperature dependence.

CHAPTER V

CONCLUSION AND FUTURE WORK

A. Summary

We have built a low temperature scanning tunneling microscope (LTSTM). It was designed to be as compact as possible in order to increase the frequencies of any internal vibration modes and to make the STM less susceptible to external vibrations. All of the construction materials were chosen to be compatible with operation in ultra high vacuum (UHV). In particular, the body of the STM is made from a single piece of titanium. Titanium was chosen because the thermal expansion coefficient of titanium is a good match to the coefficients of the piezoceramic materials and the Macor insulators and therefore the relative motion of the tip is reduced whenever the temperature of the STM is changed.

The STM was tested on an existing ^3He cryostat at different temperatures. We have analyzed the operational electronic and vibration noises of the STM. By improving the shielding of the tip holder and switching to a lower capacitance cable, we obtained a 60% reduction in the tunnel current noise. We also found that much of the current noise is caused by the motion of the tip as the tip is scanned across a surface. By adjusting some of the parameters such as the scanning speed and current setpoint in the SPM 1000 control box, one can lower this vibration noise level. The scanning speed and current setpoint are determined by the size of scan area and the roughness of the sample surface. The smaller the scan area and the smoother the sample surface, the faster the scanning speed and the larger the current setpoint can be set.

To demonstrate the capabilities of the STM, we obtained atomically resolved images of the Au (111) and graphite surfaces. With regards to the graphite surface, we typically observed the triangular sublattice consisting of only the β carbon atoms. However, 30% of the time with the same tip and bias voltage, we would observe the hexagonal lattice consisting of both the α and β atoms. This contradicts many of the proposed explanations for the observation of these two images because these explanations predict that each image requires different experimental conditions such as large or small bias voltages and/or large or small tip distances.

Finally, we showed that stable tunneling junctions can be formed between the Pt/Ir tip and a superconducting thin film PbBi. In particular, we could measure the differential conductance and observe the temperature dependence of the superconducting energy gap and density of states.

B. Piezoceramic Walker Improvements

The major difficulty in these experiments was the intermittent behavior of the piezoceramic walker. Sometimes the piezoceramic walker would not work below liquid nitrogen temperature ($\sim 50\text{ K}$). As a result, the tip would not approach the sample in a reasonable time.

We believe that the differential contraction between the titanium body and the sapphire prism may be too large and therefore the clamping force is too large for reasonable step sizes. One way to avoid this is to replace the sapphire prism with a titanium prism. To insure a smooth surface for the piezoceramic stacks, one could epoxy polished alumina plates on the sides of the prism.

Another possible explanation is that the surfaces of the piezoceramic stack pairs are not sufficiently parallel to the surface of the prism. We measured the room temperature stepsizes of all six piezoceramic stacks and found that two of them (#1 and #3) moved more slowly than the others. Furthermore, when we added additional alumina plates to four of the piezoceramic stacks in attempted to readjust the angles of the piezoceramic stacks, we found that the stepsize of only one of the slowest stacks (#1) improved but the stepsizes of stacks #3 and #5 became smaller.

We believe that to fix this problem, a new set of piezoceramic stacks must be made. To insure that the surfaces of the piezoceramic stack pairs are parallel, each piezoceramic plate of a piezoceramic stack pair should be epoxied to the Al_2O_3 bottom plate at the same time. Then the additional plates should be epoxied one layer at a time so that each of the piezoceramic stacks is parallel to the bottom plate. In addition, when the piezoceramic stack pairs are epoxied to the titanium body, the three pairs of piezoceramic stacks should be assembled with the prism and clamped with the BeCu spring so that all three pairs can be made parallel to the sapphire prism. As an additional precaution, each piezoceramic stack should be left in the vise until the epoxy is completely cured. If it should prove necessary to heat the epoxy to speed up the curing, then the entire stack and vise assembly should be heated together in an oven.

REFERENCES

- [1] G. Binnig, H. Rohrer, Surface Science 126 (1983) 236.
- [2] G. Binnig, H. Rohrer, C. Gerber, E. Weibel, Physical Review Letters 50 (1983) 120.
- [3] K. Besocke, Surface Science 181 (1987) 145.
- [4] J. W. Lyding, S. Skala, J. S. Hubacek, R. Brockenbrough, G. Gammie, Review of Scientific Instruments 59 (1988) 1897.
- [5] C. Renner, P. Niedermenn, A. D. Kent, Ø. Fischer, Review of Scientific Instruments 61 (1990) 965.
- [6] S. H. Pan, E. W. Hudson, J. C. Davis, Review of Scientific Instruments 70 (1999) 1459.
- [7] H. Hancotte, D. N. Davydov, M. Ye, R. Deltour, Physica B 204 (1995) 206.
- [8] A. D. Kent, C. Renner, P. Niedermann, J. G. Bosch, Ø. Fischer, Ultramicroscopy 42-44 (1992) 1632.
- [9] S. H. Tessmer, J. W. Lyding, D. J. van Harlingen, Review of Scientific Instruments 65 (1994) 2855.
- [10] Y. Kondo, E. T. Foley, T. Amakusa, N. Shibata, S. Chiba, M. Iwatsuki, H. Tokumoto, Review Scientific Instruments 72 (2001) 2977.
- [11] H. Zhang, U. Memmert, R. Houbertz, U. Hartmann, Review Scientific Instruments 72 (2001) 2613.

- [12] M. Kugler, C. Renner, V. Mikheev, G. Batey, Ø. Fischer, *Review Scientific Instruments* 71 (2000) 1475.
- [13] A. J. Heinrich, C. P. Lutz, J. A. Gupta, D. M. Eigler, edited by Paul M. Koenraad and Martijn Kemerink, *AIP Conf. Proc. No. 696* (2003).
- [14] J. Wiebe, A. Wachowiak, F. Meier, D. Haude, T. Foster, M. Morgenstern, R. Wiesendanger, *Review Scientific Instruments* 75 (2004) 4871.
- [15] T. Matsui, H. Kambara, H. Fukuyama, *Journal of Low Temperature Physics* 121 (2000) 803.
- [16] H. Kambara, T. Matsui, Y. Niimi, H. Fukuyama, *Review Scientific Instruments* 78 (2007) 073703.
- [17] N. Moussy, H. Courtois, B. Pannetier, *Review Scientific Instruments* 72 (2001) 128.
- [18] M. D. Upward, J. W. Janssen, L. Gurevich, A. F. Morpurgo, L. P. Kouwenhoven, *Applied Physics A: Materials Science & Processing* 72 (2001) S253.
- [19] R. J. Hamers, *Annual Review of Physical Chemistry* 40 (1989) 531.
- [20] F. Besenbacher, *Reports on Progress in Physics* 59 (1996) 1737.
- [21] N. D. Lang, *Physical Review Letters* 56 (1986) 1164.
- [22] N. D. Lang, *Physical Review Letters* 58 (1987) 45.
- [23] D. M. Eigler, P. S. Weiss, E. K. Schweizer, N. D. Lang, *Physical Review Letters* 66 (1991) 1189.

- [24] G. V. Nazin, S. W. Wu, W. Ho, Proceedings of the National Academy of Sciences 102 (2005) 8832.
- [25] F. London, H. London, Proceedings of the Royal Society of London, A149 (1935) 71.
- [26] J. D. Daunt, K. Mendelssohn, Proceedings of the Royal Society of London A185, (1946) 225.
- [27] J. Bardeen, L. N. Cooper, J. R. Schrieffer, Physical Review 108 (1957) 1175.
- [28] M. Tinkham, Introduction to Superconductivity, McGraw Hill Book Company, New York, 1975.
- [29] I. Giaever, Physical Review Letters 5 (1960) 147.
- [30] W. L. McMillan, J. M. Rowell, Physical Review Letters 14 (1965) 108.
- [31] A. L. de Lozanne, S. A. Elrod, C. F. Quate, Physical Review Letters 54 (1985) 2433.
- [32] J. R. Kirtley, S. I. Raider, R. M. Feenstra, A. P. Fein, Applied Physics Letters 50 (1987) 1607.
- [33] H. F. Hess, R. B. Robinson, R. C. Dynes, J. M. Valles, Jr., J. V. Waszczak, Physical Review Letters 62 (1989) 214.
- [34] S. H. Pan, E. W. Hudson, J. C. Davis, Applied Physics Letters 73 (1998) 2992.
- [35] J. G. Bednorz, K.A. Mueller, Zeitschrift für Physik. B64 (1986) 189.
- [36] K. M. Wu, J. R. Ashburn, C. J. Torng, P. H. Hor, R. L. Meng, et al., Physical Review Letters 58 (1987) 908.

- [37] H. Maeda, Y. Tanaka, M. Fukutumi, T. Asano, Japan, Journal of Applied Physics 27 (1988) L209.
- [38] Z. Z. Sheng, A. M. Hermann, Nature 332 (1988) 138.
- [39] C. W. Chu, Nature 365 (1993) 323.
- [40] B. C. Stipe, M. A. Rezaei, W. Ho, Review of Scientific Instruments 70 (1999) 137.
- [41] http://en.wikipedia.org/wiki/Coefficient_of_thermal_expansion/, accessed on June 20, 2010.
- [42] <http://physics.info/expansion/>, accessed on June 20, 2010.
- [43] S. H. Pan, International patent Publication No. WO 93/19494 (International Bureau, World Intellectual Property Organization), September 30, 1993.
- [44] EBL Products Inc., <http://www.eblproducts.com/>, accessed on June 20, 2010.
- [45] L. Libioulle, Y. Houbion, J. –M. Gilles, Review of Scientific Instruments 66(1) (1995) 97.
- [46] A. J. Melmed, J. Vac. Sci. Technol. B9 (1991) 601.
- [47] O. Pietzsch, A. Kubetzka, D. Haude, M. Bode, R. Wiesendanger, Review of Scientific Instruments 71 (2000) 424.
- [48] Epoxy Technology, Inc., <http://www.epotek.com/>, accessed on June 20, 2010.
- [49] MSC Industrial Direct Co., Inc., <http://www.mscdirect.com/>, accessed on June 20, 2010.
- [50] O. V. Lounasmaa, Experimental Principles and Methods Below 1K, Academic Press, New York 1974.

- [51] Mc Graw-Edison Co., <http://www.mcgraw-edison.com/>, accessed on June 20, 2010.
- [52] <http://www.eblproducts.com/piezotube.html>, accessed on June 20, 2010.
- [53] V. M. Hallmark, S. Chiang, J. F. Rabolt, J. D. Swalen, R. J. Wilson, *Physical Review Letters* 59 (1987) 2879.
- [54] C. Nogues, M. Wanunu, *Surface Science Letters* 573 (2004) L384.
- [55] I. P. Batra, N. Rohrer, H. Salemink, E. Stoll, S. Ciraci, *Surface Science* 181 (1987) 126.
- [56] H. A. Mizes, Sang-il Park, W. A. Harrison, *Physical Review B* 36 (1987) 4491.
- [57] G. Binnig, H. Fuchs, Ch. Gerber, H. Rohrer , E. Stoll E. Tosatti, *Europhysics Letters* 1 (1986) 31.
- [58] D. Tománek, S. G. Louie, H. J. Mamin, D. W. Abraham, R. E. Thomson, E. Ganz, J. Clarke, *Physical Review B* 35 (1987) 7790.
- [59] S. Hambacher, F. J. Giessibl, J. Mannhart, C. F. Quate, *Proceedings of National Academy of Sciences U.S.A.* 100 (2003) 12539.
- [60] S. Hembacher, F. J. Giessibl, J. Mannhart, *Physical Review Letters* 94 (2005) 056101.
- [61] C. D. Z. Yazdi, D. P. Pullman, *Chemical Physics* 348 (2008) 233.
- [62] M-H Whangbo, W. Liang, J. Ren, S. N. Magonov, A. Wawkuschewski, *Journal of Physical Chemistry* 98 (1994) 7602.
- [63] F. Atamny, O. Spillecke, R. Schlogl, *Physical Chemistry Chemical Physics* 1

(1999) 4113.

- [64] T. A. Land, T. Michely, R. J. Behm, J. C. Hemminger, G. Comsa, *Surface Science* 264 (1992) 261.
- [65] A. L. Tchougreeff, R. Hoffmann, *Journal of Physical Chemistry* 96 (1993) 8993.
- [66] E. Cisternas, F. Stavale, M. Flores, C. A. Achete, P. Vargas, *Physical Review B* 79 (2009) 205431.
- [67] Y. Wang, Y. Ye, K. Wu *Surface Science* 600 (2006) 729.
- [68] C. Fuchs, J. Hasse, *Zeitschrift für Physik* B28 (1977) 183.
- [69] V. M. Svistunov, A. I. D'yachenko, V. Yu. Tarenkov, *JETP Letters* 40, (10) (1984) 1252.
- [70] H. G. Le Duc, W. J. Kaiser, J. A. Stern, *Applied Physical Letters* 50 (26) (1987) 1921.
- [71] E. L. Wolf, *Principles of Electron Tunneling Spectroscopy*, Oxford, New York, 1985.

APPENDIX

PLOT PROGRAMS FOR DATA ANALYSIS

Many PLOT programs were used for data analysis and the generation of graphs.

Here are some of the most frequently used programs.

Program I_FFT.plt

!Program to plot current noise density

```

blk
er
del cv all
set dev file e:\chi_chen\data\spm_diag\aaport.eps pscfile landscape
reset variable
!variable to set scale of plot
scl=0.75

xlen=8*scl
ylen=6*scl
$ans:="y"
index=0
!ask for file
repeat

string query "WHAT IS THE FILENAME?" "$FILE" $FILE
read file "$FILE" x 1 y 3
title si .17 x .2*scl y scl*(5.8-.2*index) "$file" color (index+1)
index=index+1

string query "DO YOU WANT TO READ IN ANOTHER FILE?" "Y" $ANS
string compare "$ans" "n" nans
Until (abs(nans)==0)

y=y/20+0.5*Log10(50/1000)+log10(11.1e-9) cv all

sc cv all
axes top notick

```

```

axes right log notick
axes bottom pl 0 si .2*scl label_size .2*scl x_label "Frequency (Hz)"
axes left flip log pl 0 si .2*scl label_size .2*scl y_label "PowerDensity (A/(Hz)^(1/2))"
title si .15 x scl*6 y scl*5 "I_FFT.PLT"
Do nn=1, index
pl cv nn color nn
end do
replay

```

Program I~V.plt

!Program to plot current ~ voltage curve

```

blk
er
del cv all
set dev file e:\chi_chen\data\PbBi_J~1\aaport.eps pscfile landscape
reset variable
! variable to set scale of plot
scl=0.75
xlen=8*scl
ylen=6*scl
index=0

```

!Read files and write files' name and temperatures on the graph

```

$FILE:="60909t1.txt"
read file "$FILE" x 1 y 5
title si .17 x .2*scl y scl*(5.8-.2*index) "$file 2.09K" color (index+1)
index=index+1

```

```

$FILE:="60909am1.txt"
read file "$FILE" x 1 y 5
title si .17 x .2*scl y scl*(5.8-.2*index) "$file 3.23K" color (index+1)
index=index+1

```

```

$FILE:="60909cf1.txt"
read file "$FILE" x 1 y 5
title si .17 x .2*scl y scl*(5.8-.2*index) "$file 4.17K" color (index+1)
index=index+1

```



```

$FILE:="61009v1.txt"
read file "$FILE" x 1 y 5
title si .17 x .2*scl y scl*(5.8-.2*index) "$file 5.21K" color (index+1)
index=index+1

$FILE:="61009be1.txt"
read file "$FILE" x 1 y 5
title si .17 x .2*scl y scl*(5.8-.2*index) "$file 6.23K" color (index+1)
index=index+1

$FILE:="61209y1.txt"
read file "$FILE" x 1 y 5
title si .17 x .2*scl y scl*(5.8-.2*index) "$file 7.24K" color (index+1)
index=index+1

$FILE:="61209at1.txt"
read file "$FILE" x 1 y 3
title si .17 x .2*scl y scl*(5.8-.2*index) "$file 8.31K" color (index+1)
index=index+1

$FILE:="61109bo1.txt"
read file "$FILE" x 1 y 5
title si .17 x .2*scl y scl*(5.8-.2*index) "$file 9.04K" color (index+1)
index=index+1

y=y*1e9 cv all

sc cv all
axes top notick
axes right notick
axes bottom label_size .2*scl x_label "Bias (V)"
axes left label_size .2*scl y_label "Current (nA)"
title si .15 x scl*6 y scl*5.8 "I~V.PLT"
Do nn=1, index
pl cv nn color nn
end do
replay

```

Program dI_dV~V.plt

!Program to plot differential conductance ~ voltage curve

```

blk
er
del cv all
set dev file e:\chi_chen\data\PbBi_J~1\aaport.eps pscfile landscape
reset variable
!variable to set scale of plot
scl=0.75
xlen=8*scl
ylen=6*scl
index=0

```

! Read files and write files' name and temperatures on the graph

```

$FILE:="60909t2.txt"
read file "$FILE" x 1 y 5
title si .17 x .2*scl y scl*(5.8-.2*index) "$file 2.09K" color (index+1)
index=index+1

```

```

$FILE:="60909am2.txt"
read file "$FILE" x 1 y 5
title si .17 x .2*scl y scl*(5.8-.2*index) "$file 3.23K" color (index+1)
index=index+1

```

```

$FILE:="60909cf2.txt"
read file "$FILE" x 1 y 5
title si .17 x .2*scl y scl*(5.8-.2*index) "$file 4.17K" color (index+1)
index=index+1

```

```

$FILE:="61009v2.txt"
read file "$FILE" x 1 y 5
title si .17 x .2*scl y scl*(5.8-.2*index) "$file 5.21K" color (index+1)
index=index+1

```

```

$FILE:="61009be2.txt"
read file "$FILE" x 1 y 5
title si .17 x .2*scl y scl*(5.8-.2*index) "$file 6.23K" color (index+1)
index=index+1

```

```

$FILE:="61209y2.txt"
read file "$FILE" x 1 y 5
title si .17 x .2*scl y scl*(5.8-.2*index) "$file 7.24K" color (index+1)
index=index+1

```

```

$FILE:="61209at2.txt"
read file "$FILE" x 1 y 4
title si .17 x .2*scl y scl*(5.8-.2*index) "$file 8.31K" color (index+1)
index=index+1

```

```

$FILE:="61109bo2.txt"
read file "$FILE" x 1 y 2
title si .17 x .2*scl y scl*(5.8-.2*index) "$file 9.04K" color (index+1)
index=index+1

```

```

y=(y*(1e-9)*1.414*5)/0.3 cv all

```

```

sc cv all
axes top notick
axes right notick
axes bottom label_size .2*scl x_label "Bias (V)"
axes left label_size .2*scl y_label "Conductance (Ohm-1)"
title si .15 x scl*6 y scl*5.8 "d/dVI~V.PLT"
Do nn=1, index
pl cv nn color nn
end do
replay

```

VITA

Chi Chen received his Bachelor of Science degree in physics from the University of Science and Technology of China in July 2002. He graduated with a Ph.D. in Physics under the direction of Dr. Glenn Agnolet in August 2010. His research interests include Low Temperature Scanning Tunneling Microscope and Superconductivity Studies. He can be reached at: Department of Physics and Astronomy, Texas A&M University, College Station, Texas 77843-4242. His email address is: chenchi@gmail.com.